

1 **Tropical Sea Surface Temperatures following the Middle Miocene Climate Transition**
2 **from Laser-Ablation ICP-MS analysis of glassy foraminifera**
3

4 **Michael G. Nairn¹, Caroline H. Lear¹, Sindia M. Sosdian¹, Trevor R Bailey², and Simon**
5 **Beavington-Penney³**

6 ¹School of Earth and Environmental Sciences, Cardiff University, Cardiff, UK,

7 ²Department of Natural Sciences, Amgueddfa Cymru, National Museum Wales, Cathays Park,
8 Cardiff,

9 ³BG Group, 100 Thames Valley Park Drive, Reading, RG6 1PT, UK*

10
11 Corresponding author: Michael G. Nairn (NairnMG@cardiff.ac.uk)

12
13 *Current address: Department of Earth and Environmental Sciences, The University of
14 Manchester, Williamson Building, Oxford Road, Manchester, M13 9PL, UK.

15
16 **Key Points:**

- 17 • Laser-Ablation ICP-MS facilitates absolute sea surface temperature reconstructions using
18 foraminifera with diagenetic coatings.
- 19 • Tropical sea surface temperatures remained relatively stable at 24-31°C following the
20 Miocene Climate Transition.
- 21 • Development of an increased latitudinal temperature gradient began prior to the Late
22 Miocene Cooling.

23

24

25 Abstract

26 The mid-to-late Miocene is proposed as a key interval in the transition of the Earth's climate
27 state towards that of the modern-day. However, it remains a poorly understood interval in the
28 evolution of Cenozoic climate, and the sparse proxy-based climate reconstructions are associated
29 with large uncertainties. In particular, tropical sea surface temperature (SST) estimates largely
30 rely on the unsaturated alkenone U^k_{37} proxy, which fails to record temperatures higher than 29°C,
31 the TEX_{86} proxy which has challenges around its calibration, and Mg/Ca ratios of poorly
32 preserved foraminifera. We reconstruct robust, absolute, SSTs between 13.5 Ma and 9.5 Ma
33 from the South West Indian Ocean (paleolatitude $\sim 5.5^\circ\text{S}$) using Laser-Ablation (LA-) ICP-MS
34 microanalysis of glassy planktic foraminiferal Mg/Ca. Employing this microanalytical technique,
35 and stringent screening criteria, permits the reconstruction of paleotemperatures using
36 foraminifera which although glassy, are contaminated by authigenic coatings. Our absolute
37 estimates of 24-31°C suggest that SST in the tropical Indian Ocean was relatively constant
38 between 13.5 and 9.5 Ma, similar to those reconstructed from the tropics using the U^k_{37} alkenone
39 proxy. This finding suggests an interval of enhanced polar amplification between 10 and 7.5 Ma,
40 immediately prior to the global late Miocene Cooling.

41

42 1 Introduction

43 The mid-late Miocene is an important interval in the evolution of global climate through
44 the Cenozoic, representing a key period in the transition out of the warm, dynamic climate state
45 of the Miocene Climatic Optimum (MCO) into a more stable unipolar icehouse world (*Badger et al.*,
46 *2013*; *Foster et al.*, *2012*; *Greenop et al.*, *2014*; *Sosdian et al.*, *2018*). Despite being
47 characterized by similar to modern day atmospheric CO_2 concentrations (*Foster et al.*, *2012*;
48 *Sosdian et al.*, *2018*; *Super et al.*, *2018*), middle Miocene mean global temperatures were likely
49 significantly warmer than the modern day (*Pound et al.*, *2011*; *Rousselle et al.*, *2013*). This has
50 been used to suggest a decoupling of global temperature and atmospheric CO_2 forcing (*LaRiviere*
51 *et al.*, *2012*; *Pagani et al.*, *1999*), a characteristic which general circulation models struggle to
52 simulate (*Knorr et al.*, *2011*; *von der Heydt and Dijkstra*, *2006*). It has also been suggested that
53 the late Miocene was an additional important key step in the transition to our modern climate
54 state, as high latitudes cooled more than low latitudes, leading to a marked steepening of
55 latitudinal temperature gradients (*Herbert et al.*, *2016*).

56

57 The late Miocene Cooling (LMC) between ~ 7.5 and 5.5 Ma was a global phenomenon
58 (*Herbert et al.*, *2016*) perhaps associated with decreasing atmospheric $p\text{CO}_2$ (*Stoll et al.*, *2019*).
59 The increase in the equator to pole surface temperature gradients was not associated with an
60 increase in the benthic foraminiferal oxygen isotope record, implying that it occurred in the
61 absence of a large increase in continental ice volume (*Herbert et al.*, *2016*). Polar amplification
62 in the LMC is consistent with estimates for other time intervals (e.g., *Cramwinckel et al.* (*2018*)).
63 However, the LMC was also preceded by a significant cooling of mid to high southern and
64 northern latitudes, a heterogenous cooling at high northern latitudes, and a muted, limited
65 cooling in the tropics (*Herbert et al.*, *2016*). This heterogenous cooling perhaps suggests an
66 unusually high polar amplification factor for the interval immediately preceding the LMC.

67 Potential changes in the Earth System that could impact the magnitude of polar amplification
68 include sea ice extent, vegetation induced changes in albedo, cloud cover, or ocean-atmosphere
69 heat transport. Constraining the magnitude and timing of the steepening of latitudinal
70 temperature gradients is therefore important for understanding the factors driving the late
71 Miocene surface cooling specifically, and Earth System feedbacks more generally. Ideally, this
72 would be achieved through a combined data-modelling approach using multi-proxy temperature
73 reconstructions spanning a range of latitudes to increase confidence in calculated changes in
74 temperature gradients.

75

76 Despite the significance of this climate interval, the evolution of global sea surface
77 temperatures (SST) and hence temperature gradients during the mid-late Miocene is relatively
78 poorly constrained due to a paucity of complete well-preserved sedimentary successions (*Lunt et al.*,
79 *2008*). The widespread carbonate dissolution, which dramatically reduced the sediment
80 carbonate content and preservation quality in deep marine sediments, is termed the middle-late
81 Miocene carbonate crash (*Farrell et al.*, 1995; *Jiang et al.*, 2007; *Keller and Barron*, 1987;
82 *Lübbbers et al.*, 2019; *Lyle et al.*, 1995). In addition to these dissolution issues, the majority of
83 foraminifera-bearing Miocene sections are comprised of carbonate rich sediments which have
84 undergone some degree of recrystallisation. The oxygen isotopic composition of planktic
85 foraminifera that have undergone recrystallisation in seafloor sediments has been shown to be
86 biased to colder temperatures (*Pearson et al.*, 2001). While planktic foraminiferal Mg/Ca
87 appears to be less affected than $\delta^{18}\text{O}$, the impact of recrystallisation on reconstructed Mg/Ca sea
88 surface temperatures remains an additional source of uncertainty (*Sexton et al.*, 2006). As a
89 consequence, many mid-late Miocene absolute sea surface temperature reconstructions are
90 restricted to estimates based on the unsaturated alkenone proxy and the TEX₈₆ proxy (*Herbert et al.*,
91 *2016*; *Huang et al.*, 2007; *LaRiviere et al.*, 2012; *Rousselle et al.*, 2013; *Seki et al.*, 2012;
92 *Zhang et al.*, 2014). These records show a cooling in the late Miocene which begins around 10
93 Ma at high northern and southern latitudes. However, significant cooling in the tropics is not
94 apparent in the alkenone records until ~ 7.5 Ma, while atmospheric pCO₂ reconstructions also
95 suggest a significant decline from this time (*Sosdian et al.*, 2018; *Stoll et al.*, 2019). At face value
96 therefore, these records imply an interval of enhanced polar amplification between 10 Ma and
97 7.5 Ma in the absence of significant drawdown of CO₂ or increase in ice volume (*Herbert et al.*,
98 *2016*; *Sosdian et al.*, 2018). One significant caveat to this interpretation is that the Uk₃₇ alkenone
99 proxy becomes saturated above 28⁰C (*Müller et al.*, 1998) and the late Miocene tropical SSTs
100 prior to 7.5 Ma are at this limit (*Herbert et al.*, 2016). Therefore, an alternative interpretation of
101 the data would be that the high latitudes and the tropics cooled synchronously from ~ 10 Ma, but
102 the initial cooling in the tropics was not able to be recorded by the Uk₃₇ alkenone proxy.
103 Corroboration of the absolute Uk₃₇ alkenone temperatures by an independent proxy would
104 therefore confirm the timing of the global late Miocene Cooling and the possible interval of
105 enhanced polar amplification between 10 Ma and 7.5 Ma.

106

107 Here we present a new planktic foraminiferal Mg/Ca record from the Sunbird-1 industry
108 well cored offshore Kenya by BG Group. Critically, middle to late Miocene sediments in
109 Sunbird-1 are hemipelagic clays, which has resulted in glassy preservation of the foraminifera.
110 However, the foraminifera are coated with metal-rich authigenic coatings, which are not
111 removed by standard cleaning techniques. Planktic foraminifera were therefore analyzed by laser

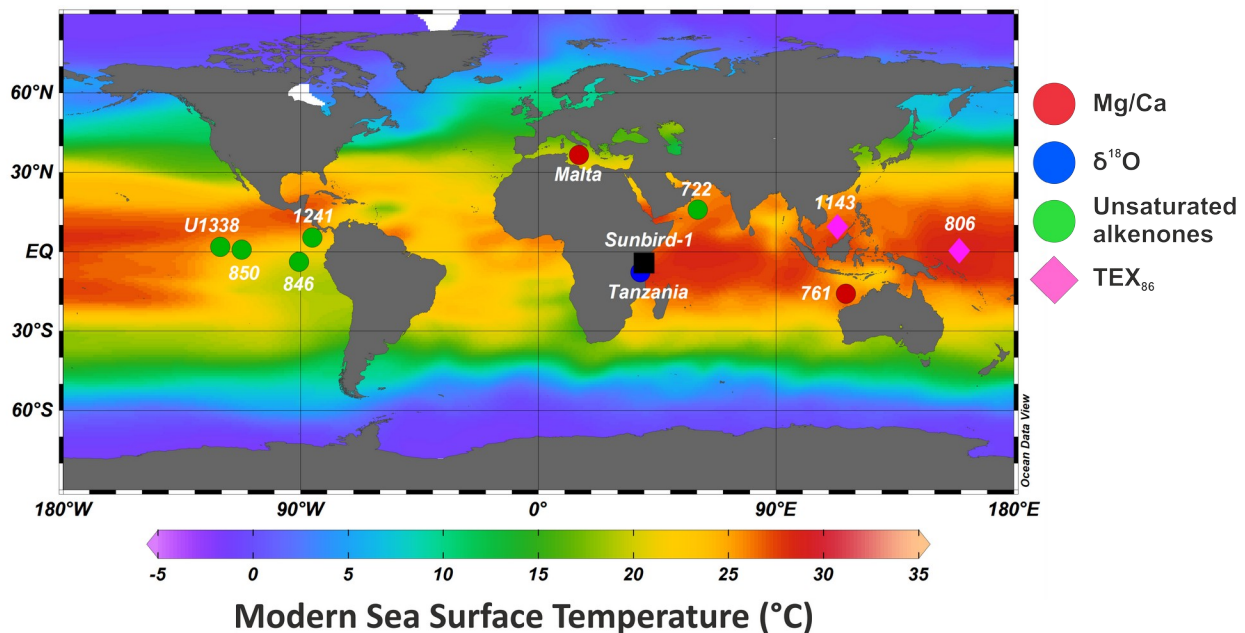
112 ablation ICP-MS to obtain Mg/Ca from the primary foraminiferal test and hence enable
 113 estimation of absolute SSTs.
 114

115 2 Materials and Methods

116 2.1 Site location, stratigraphy, and age control

117 This study utilizes 91 cuttings, spanning 273 meters at burial depths ranging from 630 m
 118 to 903 m, recovered by BG Group from the Sunbird-1 well offshore Kenya (04° 18' 13.268" S,
 119 39° 58' 29.936" E; 723.3 m water depth) (Figure 1, Supplementary Table S1). Sedimentation at
 120 Sunbird-1 through the studied interval (9.5-13.5 Ma) is dominated by clays; the fraction of the
 121 sediment >63 μ m averages 11.5% (Supplementary Table S1), much lower than typical carbonate-
 122 rich deep-water sites. The impermeable nature and chemical composition of clay-rich sediment
 123 reduces diagenetic alteration of primary foraminiferal calcite, making them ideal targets for
 124 geochemical analysis (Pearson *et al.*, 2001; Sexton *et al.*, 2006). Tests displaying the desired
 125 exceptional preservation appear glassy and translucent under reflected light, and SEM imaging
 126 shows retention of the foraminiferal original microstructure (Pearson and Burgess, 2008). This
 127 style of preferential glassy preservation, as displayed in the Sunbird-1 well, is rare to absent in
 128 published records from Miocene foraminifera.

129



130

131 **Figure 1:** Location of the Sunbird-1 study site (black square). Other sites for which there are mid
132 to late Miocene sea surface temperature reconstructions from Mg/Ca (red circles), $\delta^{18}\text{O}$ (blue
133 circles), unsaturated alkenones (green circles) and TEX_{86} (pink diamonds) are shown. Figure
134 produced using Ocean Data Viewer (*Schlitzer, R., 2018*) using modern-day mean annual sea
135 surface temperature data from the World Ocean Database.
136

137 Micropaleontological and calcareous nannoplankton assemblages for Sunbird-1 were
138 analyzed by Haydon Bailey and Liam Gallagher of Network Stratigraphic Consulting.
139 Biostratigraphic datums, correlated with the astronomical timescale of *Raffi et al. (2020)*, are
140 based on the planktic foraminifera zonations of *Wade et al. (2011)* and calcareous nanofossil
141 zonations of *Backman et al. (2012)*. An age model was constructed by linear interpolation
142 between these biostratigraphic datums (Supplementary Figure S1). Sedimentation rates were ~ 3
143 cm/kyr immediately following the middle Miocene Climate Transition (MMCT), and
144 subsequently increased to ~ 17 cm/kyr between 11.8 and 11.5 Ma, before decreasing to ~ 8 cm/kyr
145 until 9.5 Ma.
146

147 2.2 Foraminiferal stable isotope analysis

148 Up to 12 individual tests of the planktic foraminifer *Globigerinoides obliquus* showing
149 glassy preservation were used. *G. obliquus* is an extinct, symbiont-bearing species with a tropical
150 to subtropical paleogeographical distribution, and is interpreted as a surface mixed-layer dweller
151 (*Aze et al., 2011; Keller, 1985*). The assertion that *G. obliquus* inhabits and calcifies in the
152 surface mixed layer (*Aze et al., 2011; Keller, 1985*) is supported by multispecies analyses from a
153 10.0 Ma sediment sample from the Indian Ocean offshore Tanzania showing *G. obliquus* to have
154 the most negative $\delta^{18}\text{O}$ (-2.5‰) of all species (Paul Pearson, personal communication, 2019).
155 Tests were crushed between two glass plates ensuring all chambers were opened. Any visible
156 infill was removed using a fine paintbrush under a binocular microscope. Fine clays and other
157 detrital material on the outer surface of the test were removed by rinsing three times in 18.2 M Ω
158 DI water, ultrasonicing for 5-10 seconds in analytical grade methanol, and finally rinsing a
159 further time in 18.2 M Ω DI water. Samples were analyzed at Cardiff University on a
160 ThermoFinnigan MAT253 with online sample preparation using an automated Kiel IV carbonate
161 device. Results are reported relative to Vienna Pee Dee Belemnite, and long-term uncertainty
162 based on repeat analysis of NBS-19 is $\pm 0.08 \text{‰}$ ($n=469$, 2 standard deviations) and on repeat
163 analysis of BCT63 is $\pm 0.07 \text{‰}$ ($n=310$, 2 standard deviations). Data is available in
164 Supplementary Table S2.
165

166 2.3 Solution ICP-MS trace metal analysis

167 Between 10 and 15 individuals of the planktic foraminifer *Dentoglobigerina altispira*
168 from the 250 – 355 μm size fraction were picked and weighed on a six-decimal-place balance to
169 determine average test weight. Individual tests were then crushed between two glass plates
170 ensuring all chambers were opened. Due to the low foraminiferal abundance it was not possible
171 to analyze the same species for stable isotope and trace metal composition. Any visible infill was
172 removed using a fine paintbrush under a binocular microscope. Fragments were cleaned to

173 remove clays and organic matter following the standard protocol (*Barker et al.*, 2003; *Boyle and*
174 *Keigwin*, 1985). Due to the clay-rich nature of the sediment the clay removal procedure was
175 conducted twice. To test for the possible presence of metal oxides half of the samples were
176 reductively cleaned between the clay removal and oxidative cleaning steps. Samples were
177 dissolved in trace metal pure 0.065 M HNO₃ and diluted with trace metal pure 0.5M HNO₃ to a
178 final volume of 350 µl. Samples were analyzed at Cardiff University on a Thermo Element XR
179 ICP-MS using standards with matched calcium concentrations to reduce matrix effects (*Lear et*
180 *al.*, 2010; *Lear et al.*, 2002). Together with Mg/Ca, several other ratios (Al/Ca, Mn/Ca, and
181 U/Ca) were analyzed to screen for potential contaminant phases. Data are available in
182 Supplementary Table S3. Long-term analytical precision for Mg/Ca throughout the study is
183 better than 2%.
184

185 2.4 Laser ablation-ICP-MS analysis

186 Direct sampling of solid phase material via laser ablation (LA-) allows for geochemical
187 analyses through individual foraminiferal tests at the sub-micron scale when coupled to an
188 inductively-coupled-plasma mass spectrometer (ICP-MS) (*Detlef et al.*, 2019; *Eggins et al.*,
189 2004; *Evans et al.*, 2015a; *Fehrenbacher et al.*, 2015; *Hines et al.*, 2017; *Petersen et al.*, 2018;
190 *Reichart et al.*, 2003). A key advantage of analyzing the trace element composition of
191 foraminifera using LA-ICP-MS over the more traditional solution-based ICP-MS is the ability to
192 recognize the diagenetically altered portions of the tests, allowing identification of the primary
193 calcite (*Creech et al.*, 2010; *Hasenfratz et al.*, 2016; *Pena et al.*, 2005). The elemental
194 composition of this primary calcite can provide important information about palaeotemperature
195 (*Nooijer et al.*, 2017; *Eggins et al.*, 2003; *Pena et al.*, 2005) and other paleo-environmental
196 conditions such as pH (*Mayk et al.*, 2020; *Thil et al.*, 2016) and oxygenation (*Koho et al.*, 2015;
197 *Petersen et al.*, 2018).
198

199 Up to six specimens of *D. altispira* per sample were selected from 44 depth intervals
200 through the Sunbird-1 core for LA-ICP-MS analysis. Foraminiferal sample preparation included
201 the removal of fine clays and other detrital material on the outer surface of the test using DI
202 water and methanol, but the more aggressive oxidative and reductive steps (*Barker et al.*, 2003;
203 *Boyle and Keigwin*, 1985), were not required for laser ablation analysis (*Vetter et al.*, 2013). The
204 cleaned tests were mounted onto glass slides using double sided carbon tape and were allowed to
205 dry before being mounted into the sample cell (*Evans et al.*, 2015b; *Fehrenbacher et al.*, 2015;
206 *Hines et al.*, 2017).
207

208 Analyses were performed using an ArF excimer (193nm) LA- system with dual-volume
209 laser-ablation cell (RESOLUTION S-155, Australian Scientific Instruments) coupled to a Thermo
210 Element XR ICP-MS. Optimized ablation parameters and analytical settings determined for
211 analyzing foraminifera in the Cardiff University CELTIC laboratory (Supplementary Table S4;
212 (*Detlef et al.*, 2019; *Nairn*, 2018)) were used for this study. Three cleaning pulses to remove any
213 contaminant on the outer ~0.5 µm of the test surface were included prior to analysis. We
214 analyzed ²⁵Mg, ²⁷Al, ⁴³Ca, ⁵⁵Mn and ⁸⁸Sr, each isotope having a constant 50 ms dwell time.
215 Typically, intervals with elevated Mn and Al in concert with elevated Mg are interpreted as

216 being contaminant phases (e.g., Fe-Mn oxides-hydroxides or clays), and are commonly found on
217 the inner and outer test surface (*Barker et al.*, 2003; *de Nooijer et al.*, 2014; *Hasenfratz et al.*,
218 2016; *Koho et al.*, 2015; *Pena et al.*, 2005).

219

220 Where possible, three laser spot depth profiles were collected on each of the penultimate
221 (f-1) and previous (f-2) chambers by ablating with 100 consecutive laser pulses in one position
222 on the test. Assuming that each laser pulse only ablates a $\sim 0.1 \mu\text{m}$ layer of calcite (*Eggins et al.*,
223 2003), we estimate the profile to represent a transect through the test wall approximately $15 \mu\text{m}$
224 long. However, in some cases older chambers were required to ensure six laser profiles per
225 specimen were analyzed (*Nairn*, 2018). NIST SRM 610 glass standard was measured between
226 every six laser profiles, and NIST SRM 612 at the beginning and end of analyses from each
227 sample depth. The reference values for elemental concentrations in both silicate glass standards
228 are taken from the GEOREM website
229 (http://georem.mpch-mainz.gwdg.de/sample_query_pref.asp), updated from *Jochum et al.*
230 (2011a). NIST SRM 612 was used to determine long term external reproducibility using NIST
231 SRM 610. For Mg/Ca, NIST 612 (n=90) had an accuracy of 12.0% and a precision of 3.7%
232 relative to the reported value. A similar $\sim 12\%$ negative offset relative to the reported value of
233 NIST 610-calibrated NIST 612 has been observed over a much longer period of data collection
234 (*Evans and Müller*, 2018). To supplement this assessment, we also conducted accuracy tests
235 using the GOR-132 and KL-2 MPI-DING glasses (*Jochum et al.*, 2011b). For this, GOR-132 and
236 KL2 were treated as unknowns, with both NIST 610 and NIST 612 as calibration standards. For
237 Mg/Ca, GOR-132 (n=25) had an accuracy of 1.1% and a precision of 3.2% relative to the
238 reported value, and KL-2 (n=25) had an accuracy of 0.6% and a precision of 2.6% relative to the
239 reported value when calibrated using NIST 610. These values increased to 10.9% and 9.4% for
240 GOR-132, and 8.2% and 5.4% for KL-2 when calibrated using NIST 612. The NIST 610-
241 calibrated data presented here supports the determination of *Evans et al.*, (2015a) that the Mg
242 values for NIST 612 requires reassessment.

243

244 An important issue related to accuracy is that because a well-characterized, homogenous
245 calcite reference material is not currently available for laser ablation use, the glass standards we
246 used have a different matrix to the calcite foraminifera tests (*Evans et al.*, 2015a; *Evans and*
247 *Müller*, 2018; *Fehrenbacher et al.*, 2015). Therefore, while we have high confidence in the
248 accuracy of the intra-and inter-specimen geochemical variability described in Section 2.6, we
249 must consider the possibility of an analytical bias in the absolute geochemical composition of
250 foraminiferal tests determined by laser ablation ICP-MS. One way to assess the magnitude of
251 such potential bias is to analyse foraminiferal samples by both solution and laser ablation ICP-
252 MS. However, it is important to note that the corrosive cleaning protocol for solution analysis
253 tends to slightly lower primary test calcite Mg/Ca, an issue that is routinely circumvented by
254 employing the same cleaning on calibration samples for paleotemperature reconstructions
255 (*Barker et al.*, 2003). For the purpose of this study, it is therefore important that our LA-ICP-MS
256 technique gives values that are consistent with our samples analysed by solution ICP-MS. We
257 are able to make a direct comparison of our youngest samples in this way, because these do not
258 have significant authigenic coatings biasing the solution analyses. For these samples, our
259 solution and laser ablation results are in excellent agreement, which gives us confidence in the

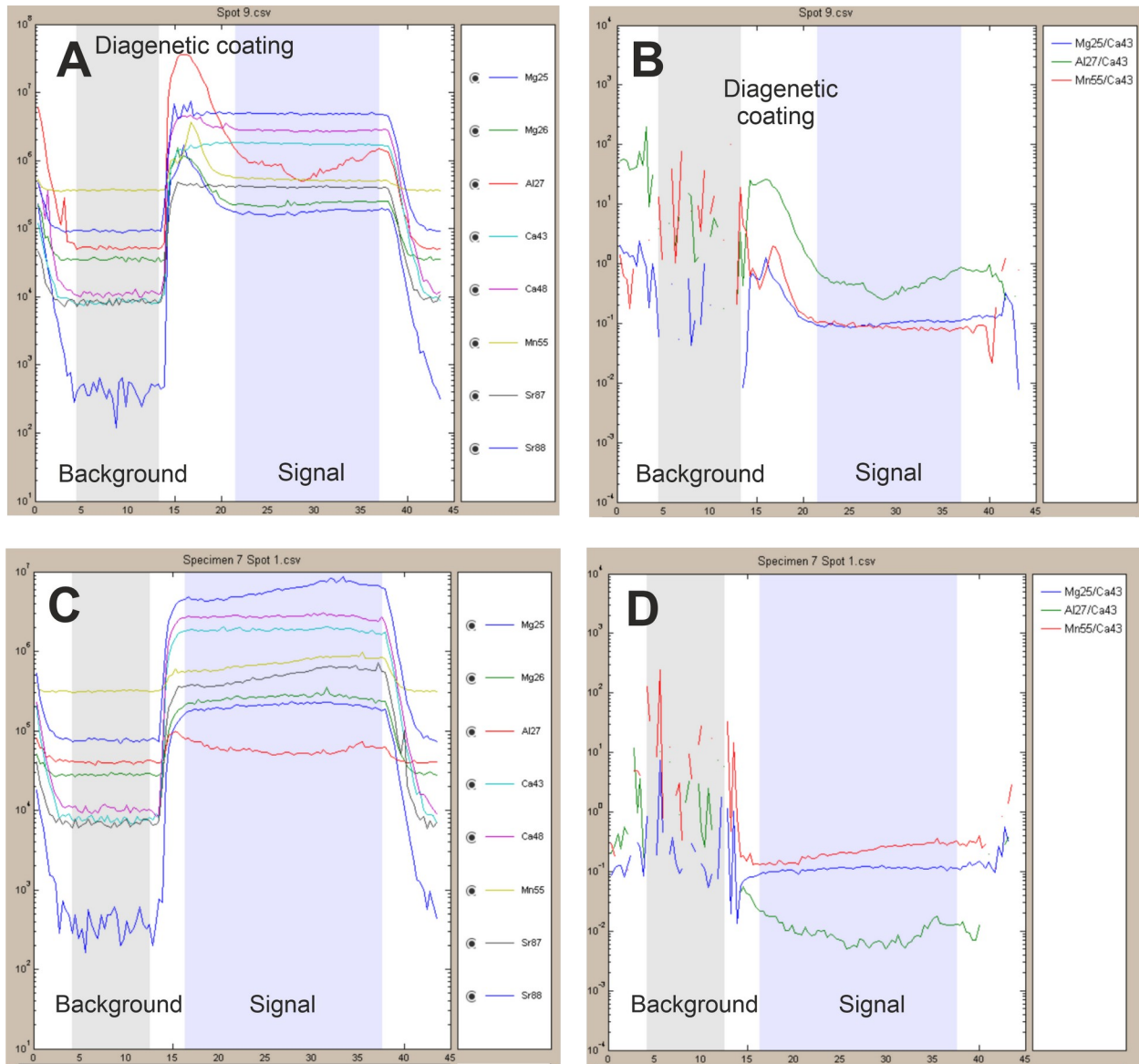
260 LA-ICP-MS values for the older samples, where we know the solution ICP-MS results are
261 compromised by authigenic coatings (Supplementary Figure S2). Furthermore, we note that if
262 future work indicates a consistent offset between laser ablation Mg/Ca analyses of carbonates
263 and silicate glasses, owing to their differing matrices, our standard values reported above will
264 allow our data to be corrected to obtain an accurate composition of the uncleaned foraminiferal
265 calcite.
266

267 2.5 LA-ICP-MS data processing and screening

268 Each individual laser ablation profile was carefully inspected and processed using the
269 SILLS data reduction software package (*Guillong et al.*, 2008) following the established protocol
270 outlined in *Longerich et al.* (1996). Profiles generally followed one of two patterns: (i) a rise
271 from background values to a transient peak, followed by a somewhat lower plateau, or (ii) a rise
272 from background values to a general plateau (Figure 2). There are two likely explanations for the
273 initial transient peak in some isotope profiles: ablation of authigenic coatings enriched in some
274 trace metals, or laser ablation induced isotope fractionation (so-called “pit effects”). We favor
275 the first explanation because we used the same operating parameters on every profile, and would
276 therefore expect any “pit effects” to be consistent among the profiles. Furthermore, profiles
277 containing the transient peaks were more prevalent in the older part of the record, where our
278 solution Mn/Ca analyses demonstrate the presence of authigenic coatings. Therefore, we assume
279 the transient peaks represent contaminated portions of the test and exclude those regions. The
280 integration interval for the profile was selected based upon the following three criteria: (i) stable
281 ^{43}Ca counts, indicating ablation of calcite, (ii) stable Mg/Ca signal, indicating a consistent
282 primary calcite phase, (iii) flat Mn/Ca and Al/Ca signals, avoiding any peaks indicating intervals
283 of contamination (Figure 2).

284

285



287 **Figure 2:** Representative LA-ICP-MS Mg, Al, and Mn profiles demonstrating the selection of
 288 background (grey panel) and sample (blue panel) signals for a profile with an authigenic coating
 289 (A, B) and for a profile without an authigenic coating (C, D). Both examples are shown in raw
 290 isotopic counts (A, C), and ratios mode (B, D) where the isotopes of interest are relative to ^{43}Ca ,
 291 the internal standard. In both examples the x axis is analysis time (seconds), and the y axis is the
 292 raw intensity of the isotopes or ratios on a log scale. The sample interval is selected to avoid the
 293 elevated Mg/Ca, Mn/Ca, and Al/Ca at the outer surface of the test.

294

295 Individual depth profiles were corrected by first subtracting the mean background signal
 296 (determined from ~ 15 seconds of data acquired when the laser was turned off prior to ablation).
 297 The repeated analysis of the NIST 610 standard reference material was used to linearly correct

298 for any instrumental drift. Typically, this is small, <2%, because of the good counting statistics
299 and stable data acquisition during ablation. The ablation profiles were normalized to ^{43}Ca as the
300 internal standard and elemental concentrations (TM/Ca) were calculated, assuming 40 wt % for
301 CaCO_3 .

302

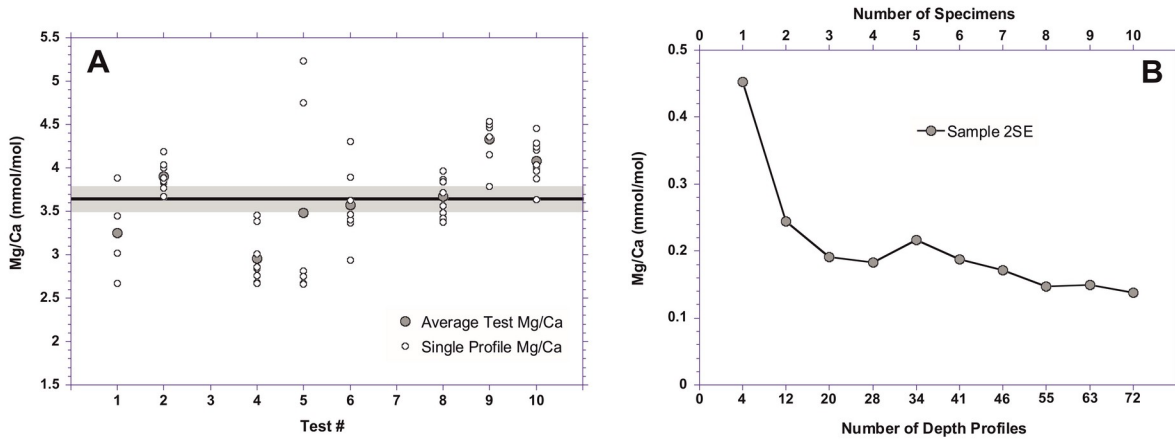
303 Following data processing, rigorous screening of the Mg/Ca ratios for the influence of
304 intratest contamination was conducted. It is important to recognise that Mn/Mg and Al/Mg of
305 contaminant phases vary greatly, such that there is no single universal threshold for these
306 elements that can be applied in every situation (*Lear et al.*, 2015). For the Sunbird-1 samples we
307 examined co-variation of Mg/Ca and Mn/Ca and chose to exclude all samples above a Mn/Ca
308 threshold of 200 $\mu\text{mol/mol}$ (Supplementary Figure S3). Consideration of Al/Ca was more
309 complex, as some samples with extremely high Al/Ca (>1000 $\mu\text{mol/mol}$) was not associated with
310 markedly elevated Mg/Ca. This result demonstrates that aluminum is sporadically present in
311 foraminiferal tests in variable phases (with differing Al/Mg). We therefore used a dual-pronged
312 approach, considering both Al/Ca and intra-sample heterogeneity. We excluded profiles where
313 two conditions were met: (i) Al/Ca was >100 $\mu\text{mol/mol}$, and (ii) the associated Mg/Ca was
314 substantially elevated relative to the other depth profiles from the same sample.

315

316 2.6 Determination of mean foraminiferal test Mg/Ca by laser ablation

317 Geochemical heterogeneity exists both within an individual foraminiferal test and
318 between foraminiferal tests from the same sample (*Eggins et al.*, 2004; *Fehrenbacher and*
319 *Martin*, 2014; *Sadekov et al.*, 2008; *Sadekov et al.*, 2005). Therefore, several laser ablation
320 profiles are required to produce a consistent Mg/Ca ratio for temperature reconstructions. Here
321 we analyzed ten depth profiles through each of ten individual *D. altispira* tests from the 1551-
322 1554 m (11.74 Ma) sample to determine representative inter-specimen variability for these
323 samples (Figure 3). Approximately one third (n=28) of the 100 depth profiles were excluded
324 during screening for elevated Al/Ca and Mn/Ca indicative of diagenetic contamination. The Mg/
325 Ca value of individual depth profiles in *D. altispira* from the 1551-1554 m sample ranges from
326 2.67 mmol/mol to 5.23 mmol/mol, with a mean of 3.63 ± 0.14 mmol/mol (n=72) (Figure 3a;
327 Supplementary Table S5). The mean Mg/Ca value from four specimens, a total of 28 profiles, is
328 3.41 ± 0.18 mmol/mol (Figure 3a). Averaging profiles from ten individual tests did therefore not
329 produce significantly better accuracy or precision than averaging profiles from four individual
330 tests (Figure 3b). Therefore, for a Mg/Ca ratio to be considered representative it must represent
331 an average of at least 28 laser ablation profiles, from at least four specimens, with the analytical
332 uncertainty (2 SE) indicating the intra- and inter-specimen variability this incorporates. To
333 account for depth profiles excluded due to contamination, where possible the number of
334 measurements per sample was increased to 36, six depth profiles per specimen and six specimens
335 per sample. This result is in line with other LA-ICP-MS studies (*Rathmann et al.*, 2004; *Sadekov*
336 *et al.*, 2008). Future studies are advised to conduct similar testing to determine the number of
337 measurements required for a mean sample Mg/Ca to be representative, as this will likely be site
338 dependent.

339



340

341 **Figure 3:** Distribution of *D. altispira* Mg/Ca values from LA-ICP-MS profiles of the 1551-1554
 342 m sample. (A) A summary of all Mg/Ca values, where open circles denote individual
 343 measurements, and filled circles denote mean Mg/Ca values for each specimen. The horizontal
 344 black line is the mean of all depth profiles from the sample, and the gray bar the ± 2 SE sample
 345 uncertainty. (B) The evolution of the sample 2 SE with increasing specimens. Only profiles that
 346 passed data screening are included ($n=72$). Data is provided in Supplementary Table S5.
 347

348 2.7 Mg/Ca paleo-sea surface temperature calculations

349 The influence of calcification temperature (T) on the Mg/Ca ratio of foraminiferal calcite
 350 can be explained by an exponential curve of general form $Mg/Ca = B \exp^{AT}$ where the pre-
 351 exponential constant (B) and exponential constant (A) are species specific (*Anand et al.*, 2003;
 352 *Lear et al.*, 2002; *Nürnberg et al.*, 1996; *Rosenthal et al.*, 1997). To convert raw Mg/Ca ratios to
 353 absolute temperatures, several secondary controls on Mg/Ca must be considered, and accounted
 354 for (*Gray et al.*, 2018; *Hollis et al.*, 2019; *Holland et al.*, 2020).

355

356 In this study we use Mg/Ca values from *D. altispira*, a near surface dweller present from
 357 the Oligocene to the Pliocene. Since this is not an extant species, we consider two approaches to
 358 calculating SST: (i) using the multi-species calibration equation from *Anand et al.* (2003) and (ii)
 359 using the *Globigerinoides ruber* Mg/Ca-SST equation and pH correction from *Evans et al.* 2016.

360

361 In scenario (i), we apply a compilation of nine modern planktic foraminifera (*Anand et al.*
 362 *et al.*, 2003). This calibration is commonly applied to extinct planktic foraminiferal species such as
 363 *D. altispira* and applies a power law relationship, where H is a constant that describes the
 364 sensitivity of $Mg/Ca_{CALCITE}$ to seawater Mg/Ca (Mg/Ca_{SW}) (*Hasiuk and Lohmann*, 2010; *Cramer*
 365 *et al.*, 2011; *Evans and Müller*, 2012) (Equation 1).

366

367 Equation 1: $Mg/Ca = \frac{B}{Mg/Ca_{SW}^{t=0^H}} \times Mg/Ca_{SW}^{t=t^H} \exp^{AT}$

368

369

370 Fluxes of Mg^{2+} and Ca^{2+} into and out of the oceans leads to secular variation in Mg/Ca_{sw} .
 371 This variability must be accounted for when determining absolute sea surface temperatures on
 372 Cenozoic timescales (Hollis *et al.*, 2019). Reconstructions of Mg/Ca_{sw} based on large benthic
 373 foraminifera (Evans *et al.*, 2018), calcite veins (Coggon *et al.*, 2010), fluid inclusions (Horita *et al.*,
 374 *et al.*, 2002), and echinoderms (Dickson, 2002) have constrained this variability through the
 375 Cenozoic (Supplementary Figure S4). The Eocene-Oligocene demonstrates relatively stable
 376 values of 2.0-2.5 mol/mol (Coggon *et al.*, 2010; Evans *et al.*, 2018). However, only one data
 377 point exists from the Miocene, through which Mg/Ca_{sw} more than doubles from ~ 2.2 mol/mol in
 378 the late Oligocene (Coggon *et al.*, 2010) to the well constrained value of 5.2 mol/mol in the
 379 modern ocean (Broecker *et al.*, 1982; Dickson, 2002; Horita *et al.*, 2002; Kısakürek *et al.*, 2008).
 380 Therefore, the method of Lear *et al.* (2015) is followed by fitting the fourth-order polynomial
 381 curve fit through the compiled Mg/Ca_{sw} proxy records (Supplementary Figure S4). We use a ± 0.5
 382 mol/mol uncertainty window in the following temperature calculations, this error envelope
 383 incorporating the majority of the spread in the proxy data.

384

385 The power law function negates the assumption that the temperature sensitivity remains
 386 constant, independent of changing Mg/Ca_{sw} through the Cenozoic era. We apply a power law
 387 constant of $H=0.41$, similar to the value applied for *T. trilobus*, a symbiont-bearing, mixed layer
 388 dweller (Delaney *et al.*, 1985; Evans and Müller, 2012). Adapting Equation 1 to include our H
 389 value, a modern-day Mg/Ca_{sw} value of 5.2 mol/mol, and the calibration constants of Anand *et al.*,
 390 (2003) derives Equation (2).

391

392

393 Equation 2:

394 $\frac{Mg}{Ca} = \frac{0.38 \pm 0.02}{5.2^{0.41}} \times Mg/Ca_{sw}^{0.41} \exp^{(0.090 \pm 0.003 \times SST)}$

395

396

397 This first calibration approach assumes that foraminiferal Mg/Ca is not influenced by
 398 changes in the carbonate system. However, studies have shown that planktic foraminiferal
 399 Mg/Ca is influenced by changes in the carbonate system, the ratio increasing with decreased pH
 400 and/or $\Delta[CO_3^{2-}]$ (Evans *et al.*, 2016; Gray and Evans, 2019; Gray *et al.*, 2018; Russell *et al.*,
 401 2004; Yu and Elderfield, 2008). However, the ultimate driver of this effect is not certain and
 402 some species are insensitive to changes in the carbonate system. Further, it has been shown that
 403 for *Orbulina universa* dissolved inorganic carbon (DIC) plays a role in test Mg/Ca variability
 404 (Holland *et al.*, 2020). We follow recent results which interpret pH, as opposed to $\Delta[CO_3^{2-}]$ or
 405 DIC, as the parameter which controls the carbonate system's influence on Mg/Ca (Evans *et al.*,
 406 2016; Gray *et al.*, 2018). Furthermore, unlike with either DIC or $\Delta[CO_3^{2-}]$, it is possible to

407 reconstruct pH through the Neogene using boron isotopes in foraminifera (*Foster and Rae, 2015;*
 408 *Greenop et al., 2014; Henehan et al., 2013; Sosdian et al., 2018*). For these reasons we use the
 409 recent Neogene boron isotope compilation of *Sosdian et al. (2018)*, which provides well
 410 constrained estimates of pH across this time interval (Supplementary Figure S5; Supplementary
 411 Table S9). Linear interpolation between these pH values allows us to estimate a mean pH value,
 412 and associated uncertainty envelope, for each Sunbird-1 sample, where the uncertainty envelope
 413 is maximum and minimum pH at the 17% and 83% confidence interval ($\sim \pm 0.06$ pH units).

414

415 Therefore, in addition to scenario (i) we also consider the approach from *Evans et al.*
 416 (2016) which corrects for pH changes using the interpolated Neogene pH record of *Sosdian et al.*
 417 (2018) (Supplementary Figure S5). Measured planktic foraminiferal Mg/Ca values are corrected
 418 for this influence of pH using the equation of *Evans et al. (2016)* (Equation 3).

419

$$420 \text{ Equation 3: } Mg/Ca_{CORRECTED} = \frac{Mg/Ca_{MEASURED}}{\frac{0.66}{1 + \exp(6.9(pH - 8.0))}} + 0.76$$

421

422 The preferred equation of *Evans et al. (2016)* is used to account for the influence of
 423 changing Mg/Ca_{sw} when estimating SST. These authors determined that the best fit to culture-
 424 derived calibration lines is when both the pre-exponential (B) and exponential (A) coefficients
 425 vary quadratically with Mg/Ca_{sw} (Equation 4 and 5).

426

$$427 \text{ Equation 4: } B = (0.019 \times Mg/Ca_{sw}^2) - (0.16 \times Mg/Ca_{sw}) + 0.804$$

$$428 \text{ Equation 5: } A = (-0.0029 \times Mg/Ca_{sw}^2) + (0.032 \times Mg/Ca_{sw})$$

429

430 We substitute these equations into the general exponential calibration, $Mg/Ca = B \exp^{AT}$,
 431 to account for changing Mg/Ca_{sw}. Although the *Evans et al. (2016)* equation is specific to *G.*
 432 *ruber*, this species inhabits a shallow water depth of 0-50m (*Schiebel and Hemleben, 2017*)
 433 similar to the inferred mixed-layer habitat depth *D. altispira* (*Aze et al., 2011*). Furthermore, as
 434 with *G. ruber*, *D. altispira* was a tropical/subtropical species, with symbionts (*Aze et al., 2011*).

435

436 Salinity can exert a secondary effect on foraminiferal Mg/Ca, sensitivity measurements
 437 from culture and core-top studies show this to be $\sim 3\text{-}5\%$ per practical salinity unit (psu) (*Gray et al., 2018;*
 438 *Hollis et al., 2019; Hönisch et al., 2013; Kısakürek et al., 2008*). In the absence of a
 439 robust, independent salinity proxy (although we do note the promise of Na/Ca (*Bertlich et al.,*
 440 *2018; Geerken et al., 2018*)) and the relatively minor effect of salinity on foraminiferal Mg/Ca,

441 this potential secondary control is not empirically accounted for. Sunbird-1 was located in a
442 coastal setting and likely experienced a highly variable hydrological cycle due to changes in the
443 position of the ITCZ making it susceptible to changes in salinity. Therefore, an error of $\pm 0.5^{\circ}\text{C}$
444 is incorporated into the final sea surface temperature estimates, equivalent to an assumed salinity
445 variability of $\sim\pm 1$ PSU.

446

447 Mg/Ca-derived sea surface temperature estimates calculated using both approaches (i)
448 and (ii) yield extremely similar trends (Supplementary Figure S6). Across the time interval of the
449 Sunbird-1 dataset (~ 13.5 Ma – 9.5 Ma) pH changes by a small amount and thus the choice of
450 approach has little influence on the Sunbird-1 absolute SST record. In our discussion below, we
451 adopt approach (i); the multi-species calibration equation from *Anand et al.* (2003) without a pH
452 correction. This approach avoids any potential species-specific effects from applying the *Evans*
453 *et al.* (2016) calibration specific to *G. ruber* to the extinct *D. altispira* used in this study.
454 Furthermore, *D. altispira* has been considered to be symbiont bearing, so may demonstrate a
455 muted response to changes in pH and insensitivity to pH changes, similar to *Trilobatus trilobus*
456 (*Gray and Evans, 2019*).

457

458 The uncertainties ($\pm 2\text{SE}$) associated with the conversion from Mg/Ca to absolute SST
459 estimates incorporate the uncertainty on the Mg/Ca_{sw} record, and the potential uncertainty due to
460 varying salinity. Additionally, scenario (i) incorporates the uncertainty in the calibration of
461 *Anand et al.* (2003) (Equation 2), and scenario (ii) using the approach of *Evans et al.* (2016)
462 incorporates the uncertainty in the pH correction. These combined are termed the calibration
463 uncertainty and are considerably greater than the independent analytical uncertainty, which only
464 incorporates the intra- and inter- specimen variability (± 2 SE). Absolute sea surface temperature
465 estimates, and associated uncertainties, calculated using approach (i) and (ii) are available in
466 Table 1 and Supplementary Table S9 respectively

467

Age (Ma)	Minimum Age (Ma)	Maximum Age (Ma)	Temperature (°C)	Maximum Temperature (°C)	Minimum Temperature (°C)	Analytical Error Only Maximum Temperature (°C)	Analytical Error Only Minimum Temperature (°C)
9.53	9.43	9.62	27.73	31.08	24.64	28.30	27.12
9.86	9.86	9.86	28.15	31.86	24.68	29.06	27.17
10.19	10.05	10.33	29.54	33.49	25.81	30.62	28.34
10.43	10.43	10.43	26.82	30.55	23.32	27.78	25.77
10.48	10.48	10.48	28.13	31.58	24.94	28.77	27.44
10.57	10.57	10.57	27.81	31.47	24.41	28.66	26.90
10.62	10.62	10.62	24.88	28.12	21.90	25.43	24.30
10.78	10.73	10.89	29.48	33.14	26.09	30.27	28.64
10.92	10.92	10.92	28.95	32.78	25.36	29.92	27.89
11.13	10.98	11.28	28.42	32.47	24.58	29.61	27.09
11.40	11.40	11.40	28.18	31.50	25.15	28.67	27.68
11.50	11.46	11.55	29.36	32.85	26.15	29.98	28.71
11.61	11.10	11.61	26.78	30.39	23.44	27.59	25.91
11.63	11.63	11.63	26.65	30.34	23.21	27.55	25.68
11.64	11.64	11.64	29.57	33.29	26.11	30.40	28.68
11.67	11.67	11.67	25.44	29.02	22.12	26.26	24.55
11.72	11.69	11.74	28.19	31.84	24.81	28.99	27.33
11.77	11.77	11.77	26.89	30.09	23.96	27.30	26.46
11.82	11.82	11.82	26.39	29.69	23.37	26.92	25.85
11.87	11.87	11.87	28.84	32.47	25.47	29.60	28.02
12.03	12.03	12.03	28.10	31.66	24.82	28.81	27.35
12.71	12.57	12.85	29.14	32.80	25.77	29.90	28.34
13.23	13.13	13.33	28.85	32.54	25.43	29.64	28.00

468

469 **Table 1.** Sunbird-1 LA-ICP-MS Mg/Ca derived SST using the approach of *Anand et al. (2003)*
470 without a pH correction. Minimum and maximum age refer to the age range of the pooled
471 samples (Supplementary Table S7). Maximum and Minimum temperatures refer to the full range
472 of absolute temperatures derived incorporating the analytical and calibration uncertainty,
473 whereas Analytical Error Only Maximum and Minimum temperatures refer to the range of
474 temperatures derived from the analytical uncertainty only.

475

476 2.8 $\delta^{18}\text{O}$ paleo-sea surface temperature calculations

477 Due to the limited sampling resolution of the trace metal data, SST is also calculated
478 using foraminiferal $\delta^{18}\text{O}$. Foraminiferal $\delta^{18}\text{O}$ ($\delta^{18}\text{O}_{\text{calcite}}$) is converted to temperature (T) using the
479 palaeotemperature equation of *Bemis et al. (1998)* (Equation 4), changes in global ice volume

480 being corrected using the $\delta^{18}\text{O}_{\text{sw}}$ value from the nearest 0.1 Myr time interval in the compilation
 481 of *Cramer et al.* (2011).

482

483 Equation 4: $\left(\delta^{18}\text{O}_{\text{calcite}} - \delta^{18}\text{O}_{\text{sw}} + 0.27\right) = -0.21 \pm 0.003 T + 3.10 \pm 0.07$

484

485 The absence of a robust, independent salinity proxy makes any quantitative attribution of
 486 its influence on foraminiferal $\delta^{18}\text{O}$ challenging. Therefore, we incorporate potential $\delta^{18}\text{O}$
 487 variability due to salinity into any temperature estimate uncertainty. Salinity of the upper water
 488 column in a $0.75^\circ \times 0.75^\circ$ grid square around the modern-day study site varies between 34.9 and
 489 35.4 PSU (*Boyer et al.*, 2013). Using the Indian Ocean $\delta^{18}\text{O}_{\text{sw}}$ -salinity relationship of *LeGrande*
 490 *and Schmidt* (2006) (Equation 5) this equates to a maximum $\delta^{18}\text{O}_{\text{sw}}$ uncertainty of $\pm 0.091\text{‰}$.
 491 Using Equation 4 this equates to a 0.4°C uncertainty in the calculated surface temperature.

492

493 Equation 5: $\delta^{18}\text{O}_{\text{sw}}(\text{SMOW}) = (0.16 \pm 0.004 \times \text{Salinity}) - 5.31 \pm 0.135$

494

495 We acknowledge the likelihood of variability in sea surface salinity in this downcore
 496 record. We use the paleolatitude calculator of *van Hinsbergen et al.* (2015) to calculate a
 497 paleolatitude for Sunbird-1 at 10 Ma of approximately 5.5°S . The latitudinal correction of
 498 *Zachos et al.* (1994) gives a $\delta^{18}\text{O}_{\text{sw}}$ of 0.1‰ . The absence of a significant offset from SMOW
 499 (0‰) suggests that this will have a negligible influence on the isotopic SST reconstructions.

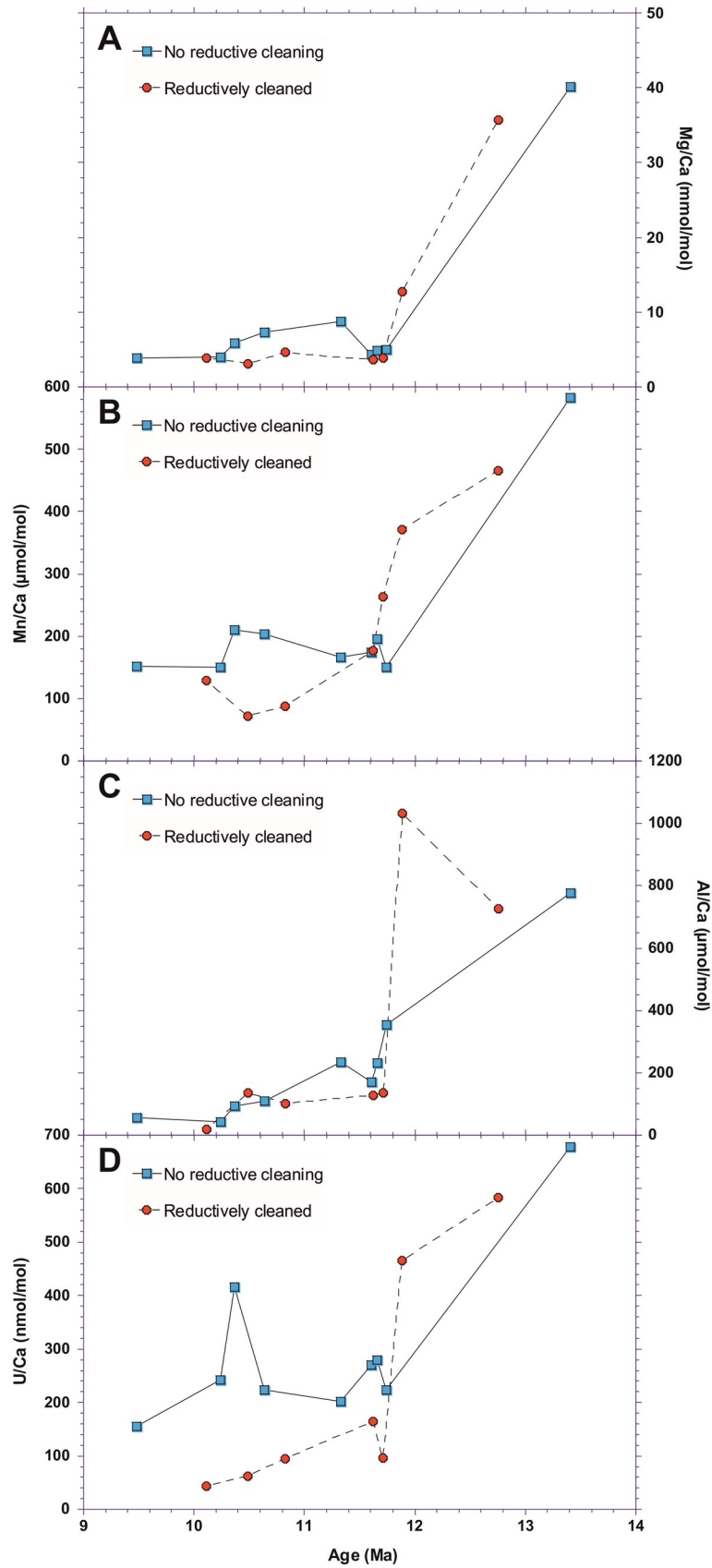
500

501 **3 Results**

502 3.1 Solution ICP-MS trace element chemistry

503 *D. altispira* Mg/Ca measured by solution ICP-MS ranges from 3.15 ± 0.1 to 40.2 ± 0.2
 504 mmol/mol (Figure 4a), translating to unrealistically high reconstructed sea surface temperatures.
 505 The high Mg/Ca ratios strongly suggest the addition of magnesium from a secondary, post-
 506 depositional source, prior to 11.75 Ma. The elevated Mg/Ca ratios are associated with
 507 correspondingly high Mn/Ca, Al/Ca, and U/Ca (Figure 4b-d). Six of the sixteen Mn/Ca ratios are
 508 in excess of the proposed $200\ \mu\text{mol/mol}$ threshold, from our LA-ICP-MS analysis, above which
 509 Mg/Ca ratios are excluded due to contamination (Supplementary Figure S3). Furthermore, every
 510 foraminiferal U/Ca ratio is considerably higher than typical U/Ca ratios of primary foraminiferal
 511 calcite, which range from $\sim 3\text{--}23\ \text{nmol/mol}$ (*Chen et al.*, 2017; *Raitzsch et al.*, 2011; *Russell et*
 512 *al.*, 2004). In addition, foraminiferal Al/Ca exceeds the commonly applied $100\ \mu\text{mol/mol}$
 513 threshold in all but the four youngest samples.

514



516 **Figure 4:** Downcore solution ICP-MS (a) Mg/Ca, (b) Mn/Ca, (c) U/Ca, and (d) Al/Ca records
517 for *D. altispira* in the Sunbird-1 core, distinguishing between sample that were reductively
518 cleaned (red circles) and those that were not (blue squares).
519

520 The presence of elevated foraminiferal Mn/Ca, Al/Ca, and U/Ca ratios does not
521 necessarily mean that the Mg/Ca ratios are contaminated. However, the downcore, point to point
522 correlation (Figure 4) and covariance (Supplementary Figure S7) between Mg/Ca and
523 contaminant indicators suggest a strong association. This downcore association between Mg/Ca
524 and contaminant indicators, despite a rigorous chemical cleaning protocol, suggests one of two
525 things; (i) the chemical cleaning protocol is not fully effective at removing contaminant coatings,
526 and/or (ii) an Mg-rich contaminant phase is pervasive throughout the calcite test.
527

528 Including the reductive cleaning step lowers Mg/Ca, Mn/Ca, and U/Ca ratios in the post
529 11.8 Ma portion of the record, but has a negligible effect on Al/Ca. Neither cleaning protocol is
530 effective at removing the authigenic coatings on the Sunbird-1 foraminifera in the pre 11.8 Ma
531 portion of the record (Figure 4). For this reason, we also analyzed Sunbird-1 planktic
532 foraminifera by laser ablation ICP-MS.
533

534 3.2 Downcore Laser Ablation ICP-MS Mg/Ca

535 Our laser ablation profiles clearly demonstrate that the metal-rich contaminant is present
536 as an authigenic surface coating on the glassy foraminifera (e.g., Figure 2a-b). Because the
537 alteration is not pervasive throughout the calcite test, laser ablation ICP-MS is an ideal approach
538 to determine primary test Mg/Ca on these coated samples (section 2.6). *D. altispira* Mg/Ca
539 determined by laser-ablation ICP-MS ranges from 3.03 to 5.07 mmol/mol, with an average value
540 of 4.18 ± 0.40 mmol/mol, and errors ($\pm 2SE$) range from 0.10 to 1.04 mmol/mol (Supplementary
541 Table S6). However, due to elevated Al/Ca and Mn/Ca ratios, only 14 of the 44 samples are
542 represented by at least 28 laser profiles. To alleviate this problem, adjacent samples have been
543 combined into longer time slices to ensure that the absolute mean Mg/Ca measurements are
544 robust (Supplementary Table S7). Samples comprising the mean of at least 28 laser profiles are
545 termed “un-pooled samples”. Samples pooled to achieve a minimum of 28 laser profiles are
546 termed “pooled samples”. It is acknowledged that combining adjacent samples, which span up to
547 420 kyr, could incorporate orbital scale climatic variability into these pooled samples. However,
548 we do not infer climatic variability on orbital timescales because the coarse sampling resolution
549 could incorporate aliasing of any precessional or obliquity periodicity into longer term
550 eccentricity cycles (*Pisias and Mix, 1988*). Combining adjacent samples to generate a
551 representative mean Mg/Ca for a longer time-slice could smooth orbital scale variability, could
552 reduce uncertainty and assist the interpretation of longer-term climatic trends.
553

554 The mean Mg/Ca of representative samples after incorporating the nine pooled Mg/Ca
555 samples with the 14 un-pooled samples ranges from 3.08 to 4.70 mmol/mol, with an average
556 value of 4.04 ± 0.29 mmol/mol, and errors ($\pm 2SE$) range from 0.14 to 0.48 mmol/mol
557 (Supplementary Table S8). These values are in good agreement with the reductively cleaned

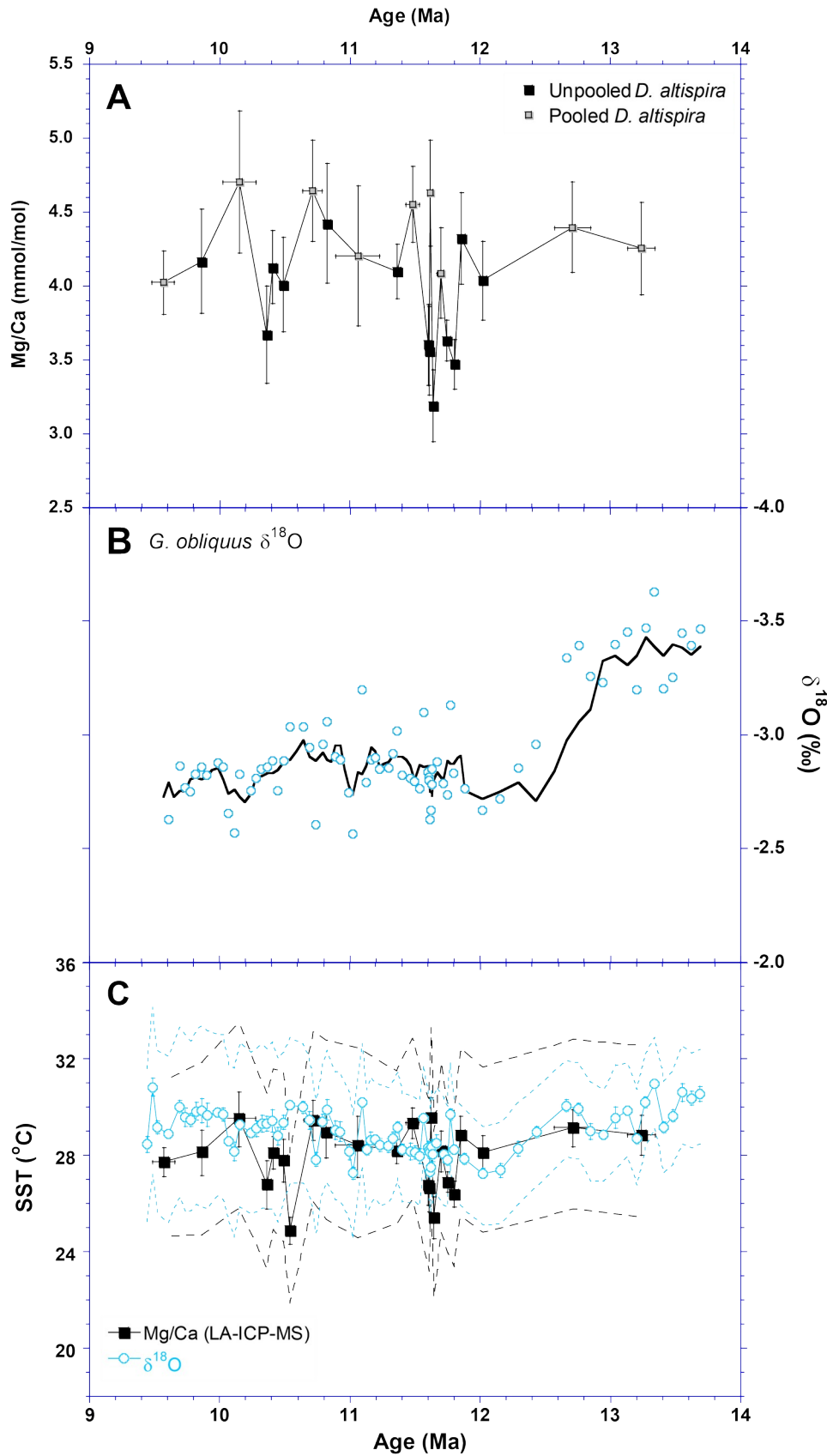
558 solution ICP-MS data for the post-11.8 Ma portion of the record (Supplementary Figure S2),
559 coinciding with the interval when contaminant indicators (Mn/Ca, Al/Ca, and U/Ca) are
560 substantially lower (Figure 4b-d). This agreement between Mg/Ca values obtained by LA-ICP-
561 MS and solution ICP-MS following effective reductive-cleaning supports the suitability of the
562 LA-ICP-MS analyses. Because we can be more confident that the laser ablation data are not
563 biased by authigenic coatings, the laser-ablation approach has the advantage that we can also
564 determine original test Mg/Ca in the older part of the record.
565

566 There is no obvious long-term trend in Mg/Ca through the interval (Figure 5a). Between
567 11.8 Ma and 11.7 Ma there is a 0.7-0.8 mmol/mol decrease in Mg/Ca followed by a recovery to
568 approximately previous values at 11.5-11.4 Ma. There is a Mg/Ca decrease of similar magnitude
569 from between 10.7 Ma and 10.36 Ma, recovering by 9.85 Ma. We acknowledge that the coarse
570 sampling frequency, and the combining of samples could be obscuring similar variability
571 through the rest of the record.
572

573 3.3 *G. obliquus* $\delta^{18}\text{O}$

574 *G. obliquus* $\delta^{18}\text{O}$ ranges from -3.63‰ to -2.34‰ with a mean value of -2.92‰. The $\delta^{18}\text{O}$
575 record shows very little variability, values remaining stable at -3.4‰ prior to a positive 0.6‰
576 shift at ~12.5 Ma, and -2.7‰ after (Figure 5b). The low variability translates to a stable $\delta^{18}\text{O}$ SST
577 record, temperatures ranging between 27°C and 31°C with the only distinctive trend being a
578 ~3°C decrease between ~12.7 Ma and 12.0 Ma. The coeval positive 0.3‰ shift in seawater $\delta^{18}\text{O}$
579 (*Cramer et al.*, 2011) dampens the influence on the SST estimate of the positive 0.6‰ shift in *G.*
580 *obliquus* $\delta^{18}\text{O}$ at ~12.5 Ma.

581



584

585 **Figure 5:** (a) Mean *D. altispira* LA-ICP-MS Mg/Ca ratios (mmol/mol) for unpooled (black
586 squares) and pooled (grey squares) samples from Sunbird-1. Error bars denote the age range for
587 pooled samples, and the $\pm 2SE$ of Mg/Ca from all depth profiles in the sample. (b) *G. obliquus*
588 $\delta^{18}O$ from Sunbird-1. Solid line is a five-point moving average. (c) Sea surface temperature
589 records at Sunbird-1 from planktic foraminiferal $\delta^{18}O$, and LA-ICP-MS Mg/Ca using our
590 preferred approach that applies the calibration of *Anand et al.* (2003) without a pH correction.
591 Symbols are the same as in (a) and (b). Error bars on the $\delta^{18}O$ record denote the analytical
592 uncertainty ($\pm 2SD$), and error bars on the Mg/Ca record denote the sample uncertainty ($\pm 2SE$).
593 As in (a), pooled Mg/Ca samples also have horizontal error bars denoting the sample age range.
594 Dashed blue and black lines denote the full uncertainty on the temperature estimates, including
595 that derived from the calibration uncertainty, for $\delta^{18}O$ and LA-ICP-MS Mg/Ca respectively.
596 Supplementary Figure S8 provides LA-ICP-MS Mg/Ca sea surface temperatures using the
597 alternative approach of *Evans et al.*, (2016).
598

599 4 Discussion

600 4.1 Reconstructing sea surface temperature from diagenetically altered foraminifera using 601 laser ablation ICP-MS

602 Robust paleotemperature reconstructions using foraminiferal Mg/Ca ratios are reliant
603 upon the Mg/Ca ratio recording a primary environmental signal, unaltered by diagenetic
604 alteration. Despite employing a thorough cleaning protocol (*Barker et al.*, 2003; *Boyle and*
605 *Keigwin*, 1985), our Mg/Ca ratios from solution-based ICP-MS analysis in the >11.8 Ma portion
606 of the record are clearly influenced by a diagenetic contaminant phase containing elevated
607 magnesium (Figure 4). This finding demonstrates that foraminifera with a glassy appearance
608 under the light microscope are not necessarily free from the influence of all modes of diagenetic
609 alteration. We therefore emphasize the importance of complementary trace metal ratios
610 indicative of contamination (i.e. Al/Ca, Mn/Ca, U/Ca) to assess the reliability of foraminiferal
611 Mg/Ca ratios (Figure 4). The application of LA-ICP-MS to collect high resolution elemental
612 profiles through the foraminiferal tests, excluding regions displaying diagenetic contamination,
613 has facilitated the identification of what we interpret to be primary paleotemperatures from
614 diagenetically altered foraminifera (*Hines et al.*, 2017; *Hollis et al.*, 2015).
615

616 The Sunbird-1 $\delta^{18}O_{PF}$ SST record from *G. obliquus* reconstructs very similar absolute
617 temperatures to the planktic foraminiferal Mg/Ca SST record (Figure 5c). Mean SST from the
618 Sunbird-1 $\delta^{18}O_{PF}$ record (29°C) is 2°C higher than mean SST from the Mg/Ca record (27°C),
619 although with the exception of the two transient decreases in Mg/Ca reconstructed SST initiating
620 at 11.8 Ma and 10.7 Ma the records are within error. The similarity of the absolute SSTs
621 reconstructed by the two proxies strengthens the case for the LA-ICP-MS Mg/Ca SST record
622 recording a primary temperature signal, and that these absolute sea surface temperatures at
623 Sunbird-1 should be considered primary.

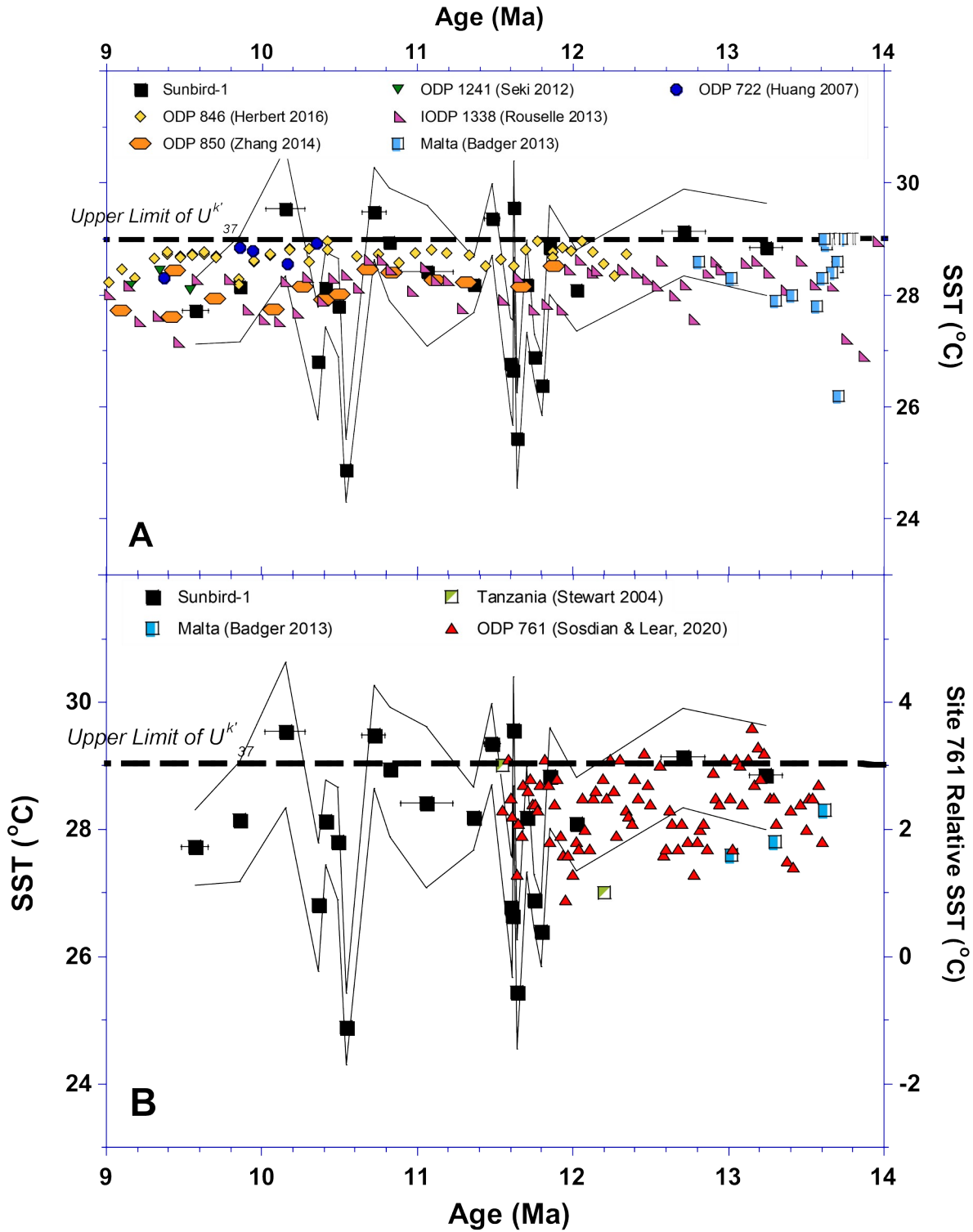
624

625 The majority of the uncertainty in the absolute temperature estimates is derived from the
626 uncertainties incorporated from the relevant calibrations, in particular the seawater Mg/Ca and
627 seawater $\delta^{18}\text{O}$ records (Figure 5c). This is true for both LA-ICP-MS Mg/Ca (Table 1 and
628 Supplementary Table S9) and $\delta^{18}\text{O}$ (Supplementary Table S10). Therefore, despite being
629 appreciable, the uncertainty resulting from the geochemical heterogeneity both within an
630 individual foraminiferal test and between foraminiferal tests from the same sample (Figure 3) is
631 not the primary contributor to the final absolute temperature uncertainty.

632

633 4.2 Mid-late Miocene sea surface temperatures in the equatorial Indian Ocean

634 The results from Sunbird-1 indicate that SST in the equatorial Indian Ocean remained
635 stable at $\sim 27^{\circ}\text{C}$ - 29°C through the 13.3 Ma to 9.5 Ma interval (Figure 5c). This finding suggests
636 that tropical climate was relatively stable following the global cooling associated with the
637 expansion of the East Antarctic Ice Sheet across the MMCT. These records from Sunbird-1
638 supports the robustness of contemporaneous alkenone based studies which exhibit similar
639 absolute tropical SST estimates (*Herbert et al.*, 2016; *Huang et al.*, 2007; *Rousselle et al.*, 2013;
640 *Seki et al.*, 2012; *Zhang et al.*, 2014) (Figure 6a). The U^{k}_{37} SST calibration fails to reconstruct
641 $\text{SST} > 29^{\circ}\text{C}$ (*Müller et al.*, 1998) but these results using Mg/Ca paleo-thermometry suggest that
642 outside the western Pacific warm pool this restriction does not apply to this time interval, unlike
643 the preceding Miocene Climatic Optimum during which Mg/Ca temperature estimates are higher
644 than those estimated with the U^{k}_{37} proxy (*Badger et al.*, 2013).



646 **Figure 6:** Sunbird-1 LA-ICP-MS Mg/Ca derived SST using the approach of *Anand et al.* (2003)
647 without a pH correction compared to and SST estimates at contemporaneous sites from (a) U^{k}_{37} ,
648 and (b) foraminiferal geochemistry. Estimates applying U^{k}_{37} are from ODP Site 722 (*Huang et al.*
649 *et al.*, 2007) in the Arabian Sea, ODP & IODP Sites 846 (*Herbert et al.*, 2016), 850 (*Zhang et al.*,
650 2014), 1241 (*Seki et al.*, 2012), and U1338 (*Rousselle et al.*, 2013) in the Eastern Equatorial
651 Pacific, terrestrial outcrops in Malta (*Badger et al.*, 2013). Estimates applying the foraminiferal
652 Mg/Ca proxy are from ODP Sites 761 (*Sosdian and Lear*, 2020) and terrestrial outcrops in Malta
653 (*Badger et al.*, 2013). ODP Site 761 data is displayed on an alternative axis as SST anomalies
654 relative to the baseline average from 16.0 – 15.5 Ma. Two temperature estimates using the $\delta^{18}O$
655 of exceptionally preserved foraminifera from Tanzania are also shown (*Stewart et al.*, 2004). The
656 upper limit for the U^{k}_{37} proxy (29°C) is marked by the thick dashed black line. All previously
657 published records used for comparison are kept on their original age models. Supplementary
658 Figure S9 provides LA-ICP-MS Mg/Ca sea surface temperatures using the alternative approach
659 of *Evans et al.*, (2016).
660

661 Although not a true tropical location, and consisting of only three data points, the *Badger*
662 *et al.* (2013) Mg/Ca record from the Mediterranean estimates SST of $\sim 27.5^{\circ}C$ between 13.5 and
663 13 Ma, within the Sunbird-1 SST uncertainty envelope (Figure 6b). Mg/Ca-SST records based
664 on less well-preserved planktic foraminifera also suggest stable tropical SST between 13.8 and
665 11.4 Ma (*Sosdian and Lear*, 2020) (Figure 6b). Furthermore, well preserved planktic
666 foraminifera from clay-rich sediments of coastal Tanzania yield Indian Ocean sea surface
667 temperatures of $27^{\circ}C$ at 12.2 Ma and $29^{\circ}C$ at 11.55 Ma using the $\delta^{18}O$ paleo-thermometer
668 (*Stewart et al.*, 2004), again in agreement with the Sunbird-1 temperature estimates (Figure 6b).
669 It is worth noting that this study, as well as the tropical SST records of *Herbert et al.* (2016) and
670 references therein, do not sample the warm pool of the Western Pacific. Sea surface temperature
671 estimates for the western equatorial Pacific using the TEX_{86} paleothermometer suggest a slight,
672 $\sim 1^{\circ}C$, SST decrease between 12 Ma and 9 Ma, whilst those for the eastern equatorial Pacific are
673 more or less constant across the same interval (*Zhang et al.*, 2014).
674

675 Although the estimates provided by the Sunbird-1 record suggest absolute tropical sea
676 surface temperatures remained relatively stable through the mid-late Miocene, some temporal
677 variability does persist. Between 11.8 Ma and 11.7 Ma SST drops sharply by $\sim 3^{\circ}C$. Excluding
678 one value of $28.6^{\circ}C$ at 11.62 Ma, this decrease in SST to $\sim 24-25^{\circ}C$ persists for ~ 300 kyr before
679 recovering to pre excursion values by 11.5 Ma. However, no transient decrease in sea surface
680 temperature is recorded from contemporaneous alkenone based estimates of tropical SST
681 utilizing the U^{k}_{37} proxy from the Arabian Sea (*Huang et al.*, 2007), and the Eastern Equatorial
682 Pacific (*Herbert et al.*, 2016; *Rousselle et al.*, 2013; *Seki et al.*, 2012; *Zhang et al.*, 2014) (Figure
683 6a). We therefore suggest that the observed transient $\sim 3^{\circ}C$ SST decrease is not the result of a
684 global driver, and supports a mechanism causing local ocean cooling of the surface waters at
685 Sunbird-1. An alternative hypothesis is that an unaccounted increase in local salinity and/or pH,
686 lowering foraminiferal Mg/Ca ratios, caused a bias to cooler temperatures between ~ 11.8 and
687 11.5 Ma. Assuming constant SST, the observed ~ 0.7 mmol/mol decrease in Mg/Ca would
688 require a salinity increase on the order of 5.0 PSU (*Hönisch et al.*, 2013; *Gray et al.*, 2018). This

689 salinity increase equates to a 0.8 ‰ change in $\delta^{18}\text{O}$ using the Indian Ocean $\delta^{18}\text{O}_{\text{sw}}$ -salinity
690 relationship of *LeGrande and Schmidt* (2006) (Equation 5). As well as being an extremely large
691 change in salinity, the planktic foraminiferal $\delta^{18}\text{O}$ record does not support such a significant
692 change in sea surface salinity between ~11.8 and 11.5 Ma (Figure 5b). However, we do
693 acknowledge that a contribution from increased salinity control cannot be discounted. Despite
694 incorporating varying pH from a globally distributed set of open ocean sites (*Sosdian et al.*,
695 2018), a localized increase in pH at Sunbird-1 cannot be ruled out. This possibility may be
696 particularly relevant considering the land-proximal, tectonically active nature of the study site. A
697 further possibility is that selective dissolution of foraminiferal chambers precipitated during
698 warmer seasons occurred during post-burial diagenetic alteration, causing an apparent ~3°C
699 lowering of SST between 11.8 Ma and 11.5 Ma. However, mean *D. altispira* test weights suggest
700 that there was no increased dissolution of the foraminiferal tests through this interval of lower
701 LA-ICP-MS Mg/Ca derived SST (Supplementary Table S11 and Supplementary Figure S10).

702

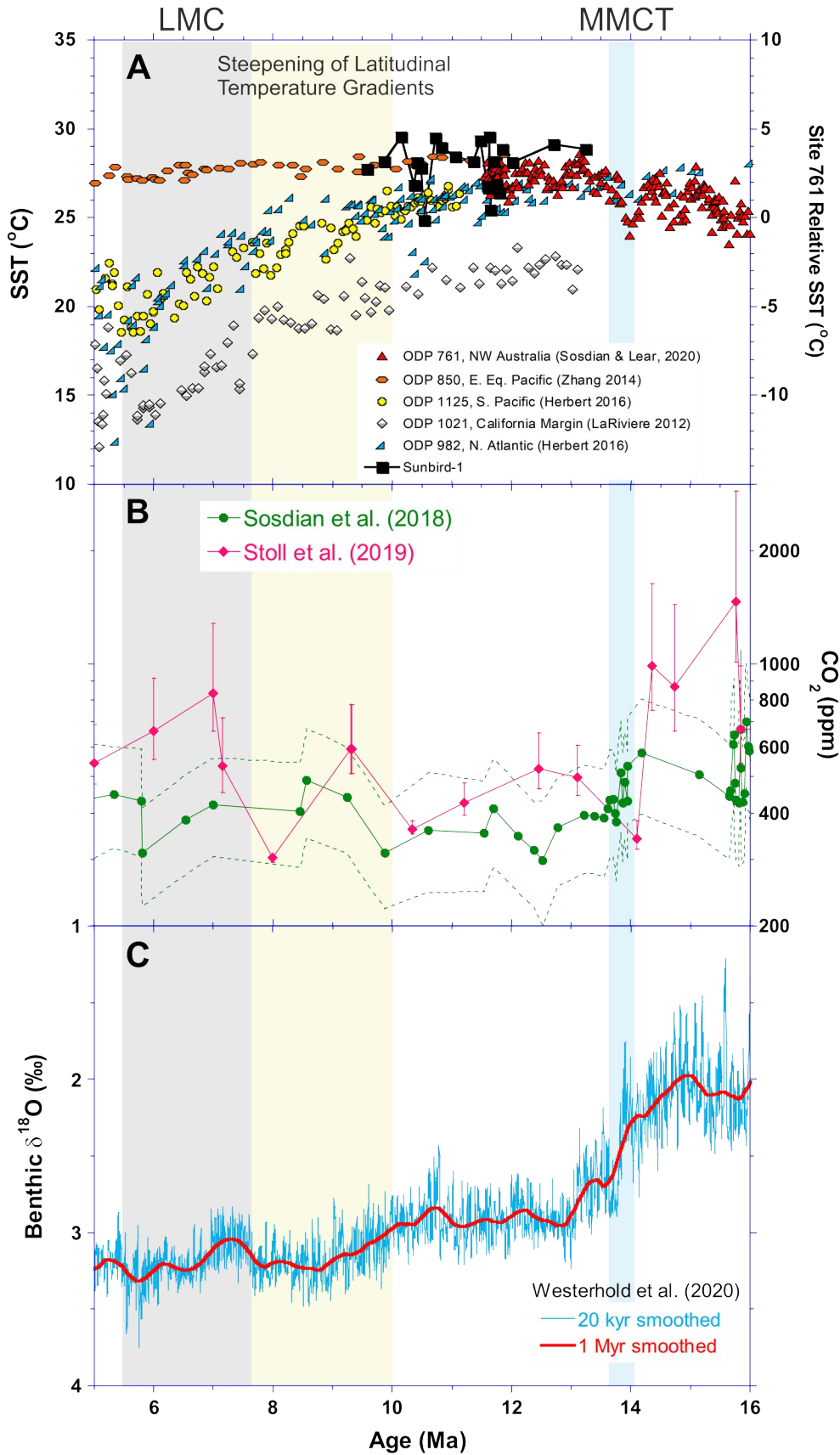
703 Therefore, our preferred interpretation is for a local cooling between ~11.8 and 11.5 Ma.
704 The lack of a marked increase in the planktic $\delta^{18}\text{O}$ record at this time implies that the cooling
705 was associated with a freshening of surface waters (Figure 5c). Interestingly, this interval
706 corresponds to a period of very high sedimentation rates (Supplementary Figure S1), which
707 might be consistent with enhanced precipitation and runoff, lowering regional surface salinity.

708

709 4.3 Implications for the global climate state during the mid-late Miocene

710 Previous studies utilizing the U^{k}_{37} proxy suggest a substantial cooling of sea surface
711 temperature at mid-to-high latitudes in both hemispheres between 10 and 5.5 Ma, whilst tropical
712 sea surface temperatures show limited cooling in the late Miocene prior to ~7 Ma (*Herbert et al.*,
713 2016; *LaRiviere et al.*, 2012). The absolute tropical SST record reported in this study supports
714 the finding that the latitudinal temperature gradient steepened from ~10 Ma, as the climate
715 system transitioned towards its modern-day state. Furthermore, support for the absolute
716 temperatures reconstructed by the alkenone proxy suggests that the interval between 10 and 7.5
717 Ma was associated with enhanced polar amplification, significantly greater than that calculated
718 for the greenhouse climate of the Eocene (*Cramwinckel et al.*, 2018). There is little evidence for
719 a significant change in pCO_2 in this interval (*Sosdian et al.*, 2018; *Stoll et al.*, 2019) (Figure 7).
720 We speculate that the marked regional cooling between 10 and 7.5 Ma perhaps reflects processes
721 internal to the climate system, involving for example ocean-atmospheric heat transport, sea ice
722 extent, or changes in regional cloud cover. A combined data-modelling approach would help
723 constrain possible factors and explore potential relationships between this highly heterogeneous
724 cooling and the CO_2 drawdown that was associated with the subsequent global late Miocene
725 Cooling starting ~7.5 Ma (Figure 7).

726



728

729 **Figure 7:** Summary of global climate through the mid-to-late Miocene. (a) Sea surface
730 temperature estimates from Sunbird-1, fellow low latitude ODP sites 850 (*Zhang et al.*, 2014)
731 and 761 (*Sosdian and Lear*, 2020), mid latitude Northern Hemisphere ODP site 1021 (*LaRiviere*
732 *et al.*, 2012), and mid-latitude Southern Hemisphere site 1125 (*Herbert et al.*, 2016), and high-
733 latitude Northern Hemisphere ODP Site 982 (*Herbert et al.*, 2016). ODP Site 761 data is
734 displayed on an alternative axis as SST anomalies relative to the baseline average from 16.0 –
735 15.5 Ma. (b) pCO₂ reconstructions, with Y axis on a log scale, of *Sosdian et al.* (2018) applying
736 the CCD reconstruction of *Pälike et al.* (2012) and the $\delta^{11}\text{B}_{\text{SW}}$ scenario of *Greenop et al.* (2017),
737 and *Stoll et al.* (2019) applying temperature estimates from *Bolton et al.* (2016) and *Zhang et al.*
738 (2013). Confidence intervals (95%) are displayed as dashed lines and error bars respectively. (c)
739 Composite benthic $\delta^{18}\text{O}$ record showing data that have been smoothed by a locally weighted
740 function over 20 kyr (blue curve) and 1 Myr (red curve) (*Westerhold et al.*, 2020). Blue, yellow,
741 and gray panels indicate intervals of ice sheet expansion across the Mid Miocene Climate
742 Transition (MMCT) associated with CO₂ decline, the steepening of latitudinal temperature
743 gradients in the absence of a CO₂ trend, and the Late Miocene Cooling (LMC).
744

745 **5 Conclusions**

746 Our Sunbird-1 sea surface temperature estimates from LA-ICP-MS Mg/Ca analyses are
747 in good agreement with those using the $\delta^{18}\text{O}$ paleo-thermometer on glassy foraminifera,
748 supporting the use of LA-ICP-MS micro-analysis across multiple specimens for reconstructing
749 paleotemperatures. This analytical technique has allowed the reconstruction of reliable Mg/Ca
750 derived paleotemperatures using foraminifera whose bulk trace element ratios demonstrate
751 diagenetic contamination by authigenic coatings. This finding opens the potential for Mg/Ca
752 paleothermometry on other challenging time intervals, and locations, where contaminant
753 coatings have previously inhibited the geochemical analysis of primary foraminiferal calcite. We
754 present new sea surface temperature records from planktic foraminiferal Mg/Ca for the south
755 west Indian Ocean between 13.5 Ma and 9.5 Ma. Absolute estimates of 24–31°C suggest that sea
756 surface temperature was relatively constant through the interval, although our record also
757 suggests two intervals of regional cooling and freshening of surface waters at 11.8 and 10.7 Ma.
758 The late Miocene represented a key interval in the transition of Earth's climate to its modern
759 state, including the development of stronger latitudinal temperature gradients. Our new
760 temperature record suggests that different mechanisms may have been responsible for this
761 cooling. The initial cooling from ~10 Ma at mid to high latitudes in both hemispheres was not
762 associated with significant cooling at low latitudes. On the other hand, the late Miocene cooling
763 between ~7.5 and 5.5 Ma was global in nature and associated with a drawdown in pCO₂. Further
764 work should therefore explore the mechanisms responsible for the enhanced polar amplification
765 between 10 and 7.5 Ma, and the possibility of carbon cycle feedbacks contributing to the
766 subsequent late Miocene Cooling.

767

768 **Acknowledgments, Samples, and Data**

769 This study uses samples from the Sunbird-1 core provided by BG-Group. All data from
770 this study can be found in Table 1 and Supplementary Tables S1 to S11, and are deposited in the
771 Zenodo online data repository <http://doi.org/10.5281/zenodo.4472994>. We thank Alexandra
772 Nederbragt and Anabel Morte-Rodeñas for laboratory assistance. We thank the reviewers and
773 editor for their insightful comments that improved the manuscript. This research was supported
774 by NERC iCASE studentship BW/22003105 (M.G.N.), and NE/L009633/1 grant to C.H.L.

775

776

777

778 **References**

- 779 Anand, P., Elderfield, H., & Conte, M. H. (2003). Calibration of Mg/Ca thermometry in
780 planktonic foraminifera from a sediment trap time series. *Paleoceanography*, 18(2).
781 <https://doi.org/10.1029/2002PA000846>
- 782 Aze, T., Ezard, T. H., Purvis, A., Coxall, H. K., Stewart, D. R., Wade, B. S., & Pearson, P. N.
783 (2011). A phylogeny of Cenozoic macroperforate planktonic foraminifera from fossil
784 data. *Biological Reviews*, 86(4), 900-927. [https://doi.org/10.1111/j.1469-](https://doi.org/10.1111/j.1469-185X.2011.00178.x)
785 [185X.2011.00178.x](https://doi.org/10.1111/j.1469-185X.2011.00178.x)
- 786 Backman, J., Raffi, I., Rio, D., Fornaciari, E., & Pälike, H. (2012). Biozonation and
787 biochronology of Miocene through Pleistocene calcareous nannofossils from low and
788 middle latitudes. *Newsletters on Stratigraphy*, 45(3), 221-244. 10.1127/0078-
789 0421/2012/0022
- 790 Badger, M. P., Lear, C. H., Pancost, R. D., Foster, G. L., Bailey, T. R., Leng, M. J., & Abels, H.
791 A. (2013). CO₂ drawdown following the middle Miocene expansion of the Antarctic Ice
792 Sheet. *Paleoceanography*, 28(1), 42-53. <https://doi.org/10.1002/palo.20015>
- 793 Barker, S., Greaves, M., & Elderfield, H. (2003). A study of cleaning procedures used for
794 foraminiferal Mg/Ca paleothermometry. *Geochemistry, Geophysics, Geosystems*, 4(9).
795 <https://doi.org/10.1029/2003GC000559>
- 796 Bemis, B. E., Spero, H. J., Bijma, J., & Lea, D. W. (1998). Reevaluation of the oxygen isotopic
797 composition of planktonic foraminifera: Experimental results and revised
798 paleotemperature equations. *Paleoceanography*, 13(2), 150-160.
799 <https://doi.org/10.1029/98PA00070>
- 800 Bertlich, J., Nürnberg, D., Hathorne, E. C., De Nooijer, L. J., Mezger, E. M., Kienast, M., et al.
801 (2018). Salinity control on Na incorporation into calcite tests of the planktonic
802 foraminifera *Trilobatus sacculifer*—evidence from culture experiments and surface
803 sediments. *Biogeosciences (BG)*, 15(20), 5991-6018. [http://dx.doi.org/10.5194/bg-2018-](http://dx.doi.org/10.5194/bg-2018-164)
804 [164](http://dx.doi.org/10.5194/bg-2018-164)
- 805 Boyer, T. P., Antonov, J. I., Baranova, O. K., Coleman, C., Garcia, H. E., Grodsky, A., et al.
806 (2013). World Ocean Database 2013.

- 807 Boyle, E., & Keigwin, L. (1985). Comparison of Atlantic and Pacific paleochemical records for
808 the last 215,000 years: Changes in deep ocean circulation and chemical inventories. *Earth*
809 *and Planetary Science Letters*, 76(1), 135-150. [http://doi.org/0012-821x/85/\\$03.30](http://doi.org/0012-821x/85/$03.30)
- 810 Boyle, E. A. (1983). Manganese carbonate overgrowths on foraminifera tests. *Geochimica et*
811 *Cosmochimica Acta*, 47(10), 1815-1819. [https://doi.org/10.1016/0016-7037\(83\)90029-7](https://doi.org/10.1016/0016-7037(83)90029-7)
- 812 Broecker, W. S., Peng, T.-H., & Beng, Z. (1982). *Tracers in the Sea*: Lamont-Doherty
813 Geological Observatory, Columbia University.
- 814 Chen, P., Yu, J., & Jin, Z. (2017). An evaluation of benthic foraminiferal U/Ca and U/Mn
815 proxies for deep ocean carbonate chemistry and redox conditions. *Geochemistry,*
816 *Geophysics, Geosystems*. Article in Press. <http://doi.org/10.1002/2016GC006730>
- 817 Coggon, R. M., Teagle, D. A., Smith-Duque, C. E., Alt, J. C., & Cooper, M. J. (2010).
818 Reconstructing past seawater Mg/Ca and Sr/Ca from mid-ocean ridge flank calcium
819 carbonate veins. *Science*, 327(5969), 1114-1117. <http://doi.org/10.1126/science.1182252>
- 820 Cramer, B., Miller, K., Barrett, P., & Wright, J. (2011). Late Cretaceous–Neogene trends in deep
821 ocean temperature and continental ice volume: reconciling records of benthic
822 foraminiferal geochemistry ($\delta^{18}\text{O}$ and Mg/Ca) with sea level history. *Journal of*
823 *Geophysical Research: Oceans (1978–2012)*, 116(C12).
824 <https://doi.org/10.1029/2011JC007255>
- 825 Cramwinckel, M. J., Huber, M., Kocken, I. J., Agnini, C., Bijl, P. K., Bohaty, S. M., et al.
826 (2018). Synchronous tropical and polar temperature evolution in the Eocene. *Nature*,
827 559(7714), 382-386. <http://doi.org/10.1038/s41586-018-0272-2>
- 828 Creech, J. B., Baker, J. A., Hollis, C. J., Morgans, H. E. G., & Smith, E. G. C. (2010). Eocene
829 sea temperatures for the mid-latitude southwest Pacific from Mg/Ca ratios in planktonic
830 and benthic foraminifera. *Earth and Planetary Science Letters*, 299(3–4), 483-495. <http://dx.doi.org/10.1016/j.epsl.2010.09.039>
- 832 de Nooijer, L. J., Hathorne, E. C., Reichart, G.-J., Langer, G., & Bijma, J. (2014). Variability in
833 calcitic Mg/Ca and Sr/Ca ratios in clones of the benthic foraminifer *Ammonia tepida*.
834 *Marine Micropaleontology*, 107, 32-43. <https://doi.org/10.1016/j.marmicro.2014.02.002>
- 835 de Nooijer, L. J., van Dijk, I., Toyofuku, T., & Reichart, G. J. (2017). The Impacts of Seawater
836 Mg/Ca and Temperature on Element Incorporation in Benthic Foraminiferal Calcite.
837 *Geochemistry, Geophysics, Geosystems*, 18(10), 3617-3630.
838 <http://doi.org/10.1002/2017GC007183>
- 839 Delaney, M. L., Be, A. W. H., & Boyle, E. A. (1985). Li, Sr, Mg, and Na in foraminiferal calcite shells from laboratory culture
840 sediment traps, and sediment cores. *Geochim. Cosmochim. Acta*, 49(6), 1327-1341.
841 [https://doi.org/10.1016/0016-7037\(85\)90284-4](https://doi.org/10.1016/0016-7037(85)90284-4)
- 842 Detlef, H., Sosdian, S. M., Kender, S., Lear, C. H., & Hall, I. R. (2019). Multi-elemental
843 composition of authigenic carbonates in benthic foraminifera from the eastern Bering Sea
844 continental margin (International Ocean Discovery Program Site U1343). *Geochimica et*
845 *Cosmochimica Acta*. <https://doi.org/10.1016/j.gca.2019.09.025>
- 846 Dickson, J. A. D. (2002). Fossil Echinoderms As Monitor of the Mg/Ca Ratio of Phanerozoic
847 Oceans. *Science*, 298(5596), 1222-1224. <http://doi.org/10.1126/science.1075882>

- 848 Eggins, S., De Deckker, P., & Marshall, J. (2003). Mg/Ca variation in planktonic foraminifera
849 tests: implications for reconstructing palaeo-seawater temperature and habitat migration.
850 *Earth and Planetary Science Letters*, 212(3), 291-306. [https://doi.org/10.1016/S0012-](https://doi.org/10.1016/S0012-821X(03)00283-8)
851 [821X\(03\)00283-8](https://doi.org/10.1016/S0012-821X(03)00283-8)
- 852 Eggins, S. M., Sadekov, A., & De Deckker, P. (2004). Modulation and daily banding of Mg/Ca
853 in *Orbulina universa* tests by symbiotic photosynthesis and respiration: a complication for
854 seawater thermometry? *Earth and Planetary Science Letters*, 225(3), 411-419.
855 <https://doi.org/10.1016/j.epsl.2004.06.019>
- 856 Evans, D. and Müller, W. (2012). Deep time foraminifera Mg/Ca paleothermometry: Nonlinear
857 correction for secular change in seawater Mg/Ca. *Paleoceanography*, 27(4).
858 <https://doi.org/10.1029/2012PA002315>
- 859 Evans, D., Erez, J., Oron, S. and Müller, W., (2015a). Mg/Ca-temperature and seawater-test
860 chemistry relationships in the shallow-dwelling large benthic foraminifera *Operculina*
861 *ammonoides*. *Geochimica et Cosmochimica Acta*, 148, pp.325-342.
862 <https://doi.org/10.1016/j.gca.2014.09.039>
- 863 Evans, D., Bhatia, R., Stoll, H., & Müller, W. (2015b). LA-ICPMS Ba/Ca analyses of planktic
864 foraminifera from the Bay of Bengal: Implications for late Pleistocene orbital control on
865 monsoon freshwater flux. *Geochemistry, Geophysics, Geosystems*, 16(8), 2598-2618.
866 <https://doi.org/10.1002/2015GC005822>
- 867 Evans, D., Brierley, C., Raymo, M. E., Erez, J., & Müller, W. (2016). Planktic foraminifera shell
868 chemistry response to seawater chemistry: Pliocene-Pleistocene seawater Mg/Ca,
869 temperature and sea level change. *Earth and Planetary Science Letters*. Article in Press.
870 <http://doi.org/10.1016/j.epsl.2016.01.013>
- 871 Evans, D., & Müller, W. (2018). Automated Extraction of a Five-Year LA-ICP-MS Trace
872 Element Dataset of Ten Common Glass and Carbonate Reference Materials: Long-Term
873 Data Quality, Optimisation and Laser Cell Homogeneity. *Geostandards and*
874 *Geoanalytical Research*. <https://doi.org/10.1111/ggr.12204>
- 875 Evans, D., Sagoo, N., Renema, W., Cotton, L. J., Müller, W., Todd, J. A., et al. (2018). Eocene
876 greenhouse climate revealed by coupled clumped isotope-Mg/Ca thermometry.
877 *Proceedings of the National Academy of Sciences of the United States of America*,
878 115(6), 1174-1179. Article. <http://doi.org/10.1073/pnas.1714744115>
- 879 Evans, D., Wade, B. S., Henahan, M., Erez, J., & Müller, W. (2016). Revisiting carbonate
880 chemistry controls on planktic foraminifera Mg / Ca: Implications for sea surface
881 temperature and hydrology shifts over the Paleocene-Eocene Thermal Maximum and
882 Eocene-Oligocene transition. *Climate of the Past*, 12(4), 819-835. Article.
883 <http://doi.org/10.5194/cp-12-819-2016>
- 884 Farrell, J. W., Raffi, I., Janecek, T. R., Murray, D. W., Levitan, M., Dadey, K. A., et al. (1995).
885 35. LATE NEOGENE SEDIMENTATION PATTERNS IN THE EASTERN
886 EQUATORIAL PACIFIC OCEAN1.
- 887 Fehrenbacher, J. S., & Martin, P. A. (2014). Exploring the dissolution effect on the intrashell
888 Mg/Ca variability of the planktic foraminifer *Globigerinoides ruber*. *Paleoceanography*,
889 29(9), 854-868. <https://doi.org/10.1002/2013PA002571>

- 890 Fehrenbacher, J. S., Spero, H. J., Russell, A. D., Vetter, L., & Eggins, S. (2015). Optimizing LA-
891 ICP-MS analytical procedures for elemental depth profiling of foraminifera shells.
892 *Chemical Geology*, 407-408, 2-9. <http://doi.org/10.1016/j.chemgeo.2015.04.007>
- 893 Foster, G. L., Lear, C. H., & Rae, J. W. B. (2012). The evolution of pCO₂, ice volume and
894 climate during the middle Miocene. *Earth and Planetary Science Letters*, 341–344(0),
895 243-254. <http://dx.doi.org/10.1016/j.epsl.2012.06.007>
- 896 Foster, G. L., & Rae, J. W. (2015). Reconstructing Ocean pH with Boron Isotopes in
897 Foraminifera. *Annual Review of Earth and Planetary Sciences*(0).
898 https://www.annualreviews.org/doi/full/10.1146/annurev-earth-060115-012226#_i63
- 899 Geerken, E., De Nooijer, L. J., Van Dijk, I., & Reichart, G.-J. (2018). Impact of salinity on
900 element incorporation in two benthic foraminiferal species with contrasting magnesium
901 contents. *Biogeosciences*, 15(7), 2205-2218. <https://doi.org/10.5194/bg-15-2205-2018>
902
- 903 Gray, W. R., & Evans, D. (2019). Nonthermal influences on Mg/Ca in planktonic foraminifera: a
904 review of culture studies and application to the Last Glacial Maximum.
905 *Paleoceanography and Paleoclimatology*, 34(3), 306-315.
906 <https://doi.org/10.1029/2018PA003517>
- 907 Gray, W. R., Weldeab, S., Lea, D. W., Rosenthal, Y., Gruber, N., Donner, B., & Fischer, G.
908 (2018). The effects of temperature, salinity, and the carbonate system on Mg/Ca in
909 *Globigerinoides ruber* (white): A global sediment trap calibration. *Earth and Planetary*
910 *Science Letters*, 482, 607-620. Article. <http://doi.org/10.1016/j.epsl.2017.11.026>
- 911 Greenop, R., Foster, G. L., Wilson, P. A., & Lear, C. H. (2014). Middle Miocene climate
912 instability associated with high-amplitude CO₂ variability. *Paleoceanography*, 29(9),
913 845-853. <https://doi.org/10.1002/2014PA002653>
- 914 Greenop, R., Hain, M. P., Sosdian, S. M., Oliver, K. I. C., Goodwin, P., Chalk, T. B., et al.
915 (2017). A record of Neogene seawater δ¹¹B reconstructed from paired δ¹¹B analyses on
916 benthic and planktic foraminifera. *Climate of the Past*, 13(2), 149-170. Article.
917 <https://doi.org/10.5194/cp-13-149-2017>
- 918 Guillong, M., L. Meier, D., Allan, M., A. Heinrich, C., & Yardley, B. (2008). *SILLS: A*
919 *MATLAB-based program for the reduction of laser ablation ICP-MS data of*
920 *homogeneous materials and inclusions* (Vol. 40).
- 921 Hasenfratz, A. P., Martínez-García, A., Jaccard, S. L., Vance, D., Wälle, M., Greaves, M., &
922 Haug, G. H. (2016). Determination of the Mg/Mn ratio in foraminiferal coatings: An
923 approach to correct Mg/Ca temperatures for Mn-rich contaminant phases. *Earth and*
924 *Planetary Science Letters*. <http://dx.doi.org/10.1016/j.epsl.2016.10.004>
- 925 Hasiuk, F.J. and Lohmann, K.C., 2010. Application of calcite Mg partitioning functions to the
926 reconstruction of paleocean Mg/Ca. *Geochimica et Cosmochimica Acta*, 74(23),
927 pp.6751-6763. <https://doi.org/10.1016/j.gca.2010.07.030>
- 928 Henehan, M. J., Rae, J. W. B., Foster, G. L., Erez, J., Prentice, K. C., Kucera, M., et al. (2013).
929 Calibration of the boron isotope proxy in the planktonic foraminifera *Globigerinoides*

- 930 ruber for use in palaeo-CO₂ reconstruction. *Earth and Planetary Science Letters*, 364,
931 111-122. <https://doi.org/10.1016/j.epsl.2012.12.029>
- 932 Herbert, T. D., Lawrence, K. T., Tzanova, A., Peterson, L. C., Caballero-Gill, R., & Kelly, C. S.
933 (2016). Late Miocene global cooling and the rise of modern ecosystems. *Nature*
934 *Geoscience*. <https://doi.org/10.1038/ngeo2813>
- 935 Hines, B. R., Hollis, C. J., Atkins, C. B., Baker, J. A., Morgans, H. E. G., & Strong, P. C. (2017).
936 Reduction of oceanic temperature gradients in the early Eocene Southwest Pacific Ocean.
937 *Palaeogeography, Palaeoclimatology, Palaeoecology*, 475, 41-54.
938 <https://doi.org/10.1016/j.palaeo.2017.02.037>
- 939 Holland, K., Branson, O., Haynes, L. L., Hönisch, B., Allen, K. A., Russell, A. D., et al. (2020).
940 Constraining multiple controls on planktic foraminifera Mg/Ca. *Geochimica et*
941 *Cosmochimica Acta*, 273, 116-136. Article. <https://doi.org/10.1016/j.gca.2020.01.015>
- 942 Hollis, C., Dunkley Jones, T., Anagnostou, E., Bijl, P., Cramwinckel, M., Cui, Y., et al. (2019).
943 The DeepMIP contribution to PMIP4: methodologies for selection, compilation and
944 analysis of latest Paleocene and early Eocene climate proxy data, incorporating version
945 0.1 of the DeepMIP database. *Geoscientific Model Development Discussions*, 2019, 1-98.
946 <http://dx.doi.org/10.5194/gmd-12-3149-2019>
- 947 Hollis, C., Hines, B., Littler, K., Villasante-Marcos, V., Kulhanek, D., Strong, C., et al. (2015).
948 The Paleocene–Eocene Thermal Maximum at DSDP Site 277, Campbell Plateau,
949 southern Pacific Ocean. <https://doi.org/10.5194/cp-11-1009-2015>
- 950 Hönisch, B., Allen, K. A., Lea, D. W., Spero, H. J., Eggins, S. M., Arbuszewski, J., et al. (2013).
951 The influence of salinity on Mg/Ca in planktic foraminifers—Evidence from cultures,
952 core-top sediments and complementary $\delta^{18}\text{O}$. *Geochimica et Cosmochimica Acta*, 121,
953 196-213. <https://doi.org/10.1016/j.gca.2013.07.028>
- 954 Horita, J., Zimmermann, H., & Holland, H. D. (2002). Chemical evolution of seawater during the
955 Phanerozoic: Implications from the record of marine evaporites. *Geochimica et*
956 *Cosmochimica Acta*, 66(21), 3733-3756. [https://doi.org/10.1016/S0016-7037\(01\)00884-5](https://doi.org/10.1016/S0016-7037(01)00884-5)
- 957 Huang, Y., Clemens, S. C., Liu, W., Wang, Y., & Prell, W. L. (2007). Large-scale hydrological
958 change drove the late Miocene C4 plant expansion in the Himalayan foreland and
959 Arabian Peninsula. *Geology*, 35(6), 531-534. <https://doi.org/10.1130/G23666A.1>
- 960 Hut, G. (1987). Consultants' group meeting on stable isotope reference samples for geochemical
961 and hydrological investigations.
- 962 Jiang, S., Wise, S., & Wang, Y. (2007). *Cause of the middle/late Miocene carbonate crash:*
963 *dissolution or low productivity*. Paper presented at the Proceedings of the Ocean Drilling
964 Program. Scientific Results.
- 965 Jochum, K. P., Weis, U., Stoll, B., Kuzmin, D., Yang, Q., Raczek, I., et al. (2011a).
966 Determination of reference values for NIST SRM 610–617 glasses following ISO
967 guidelines. *Geostandards and Geoanalytical Research*, 35(4), 397-429.
968 <https://doi.org/10.1111/j.1751-908X.2011.00120.x>
- 969 Jochum, K.P., Wilson, S.A., Abouchami, W., Amini, M., Chmeleff, J., Eisenhauer, A., Hegner,
970 E., Iaccheri, L.M., Kieffer, B., Krause, J. and McDonough, W.F., (2011b). GSD-1G and

- 971 MPI-DING reference glasses for in situ and bulk isotopic determination. *Geostandards*
972 and *Geoanalytical Research*, 35(2), pp.193-226. <https://doi.org/10.1111/j.1751->
973 [908X.2010.00114.x](https://doi.org/10.1111/j.1751-908X.2010.00114.x)
- 974 Keller, G. (1985). Depth stratification of planktonic foraminifers in the Miocene ocean. *The*
975 *Miocene ocean: paleoceanography and biogeography*, 163, 177-196.
- 976 Keller, G., & Barron, J. A. (1987). Paleodepth distribution of Neocene deep-sea hiatuses.
977 *Paleoceanography*, 2(6), 697-713. <https://doi.org/10.1029/PA002i006p00697>
- 978 Kısakürek, B., Eisenhauer, A., Böhm, F., Garbe-Schönberg, D., & Erez, J. (2008). Controls on
979 shell Mg/Ca and Sr/Ca in cultured planktonic foraminiferan, *Globigerinoides ruber*
980 (white). *Earth and Planetary Science Letters*, 273(3-4), 260-269.
981 <https://doi.org/10.1016/j.epsl.2008.06.026>
- 982 Knorr, G., Butzin, M., Micheels, A., & Lohmann, G. (2011). A warm Miocene climate at low
983 atmospheric CO₂ levels. *Geophysical Research Letters*, 38(20).
984 <https://doi.org/10.1029/2011GL048873>
- 985 Koho, K., de Nooijer, L., & Reichart, G. (2015). Combining benthic foraminiferal ecology and
986 shell Mn/Ca to deconvolve past bottom water oxygenation and paleoproductivity.
987 *Geochimica et Cosmochimica Acta*, 165, 294-306.
988 <https://doi.org/10.1016/j.gca.2015.06.003>
- 989 LaRiviere, J. P., Ravelo, A. C., Crimmins, A., Dekens, P. S., Ford, H. L., Lyle, M., & Wara, M.
990 W. (2012). Late Miocene decoupling of oceanic warmth and atmospheric carbon dioxide
991 forcing. *Nature*, 486(7401), 97. <https://doi.org/10.1038/nature11200>
- 992 Lear, C. H., Coxall, H. K., Foster, G. L., Lunt, D. J., Mawbey, E. M., Rosenthal, Y., et al. (2015).
993 Neogene ice volume and ocean temperatures: Insights from infaunal foraminiferal Mg/Ca
994 paleothermometry. *Paleoceanography*. <https://doi.org/10.1002/2015PA002833>
- 995 Lear, C. H., Mawbey, E. M., & Rosenthal, Y. (2010). Cenozoic benthic foraminiferal Mg/Ca and
996 Li/Ca records: Toward unlocking temperatures and saturation states. *Paleoceanography*,
997 25(4). <https://doi.org/10.1029/2009pa001880>
- 998 Lear, C. H., Rosenthal, Y., & Slowey, N. (2002). Benthic foraminiferal Mg/Ca-
999 paleothermometry: A revised core-top calibration. *Geochimica et Cosmochimica Acta*,
1000 66(19), 3375-3387. [https://doi.org/10.1016/S0016-7037\(02\)00941-9](https://doi.org/10.1016/S0016-7037(02)00941-9)
- 1001 LeGrande, A. N., & Schmidt, G. A. (2006). Global gridded data set of the oxygen isotopic
1002 composition in seawater. *Geophysical Research Letters*, 33(12).
1003 <https://doi.org/10.1029/2006GL026011>
- 1004 Lemarchand, D., Gaillardet, J., Lewin, E., & Allegre, C. (2002). Boron isotope systematics in
1005 large rivers: implications for the marine boron budget and paleo-pH reconstruction over
1006 the Cenozoic. *Chemical Geology*, 190(1), 123-140. <https://doi.org/10.1016/S0009->
1007 [2541\(02\)00114-6](https://doi.org/10.1016/S0009-2541(02)00114-6)
- 1008 Longerich, H. P., Jackson, S. E., & Günther, D. (1996). Inter-laboratory note. Laser ablation
1009 inductively coupled plasma mass spectrometric transient signal data acquisition and
1010 analyte concentration calculation. *Journal of analytical atomic spectrometry*, 11(9), 899-
1011 904. <https://doi.org/10.1039/JA9961100899>

- 1012 Lübbers, J., Kuhnt, W., Holbourn, A. E., Bolton, C. T., Gray, E., Usui, Y., et al. (2019). The
1013 middle to late Miocene “Carbonate Crash” in the equatorial Indian Ocean.
1014 *Paleoceanography and Paleoclimatology*, 34(5), 813-832.
1015 <https://doi.org/10.1029/2018PA003482>
- 1016 Lunt, D. J., Flecker, R., Valdes, P. J., Salzmann, U., Gladstone, R., & Haywood, A. M. (2008). A
1017 methodology for targeting palaeo proxy data acquisition: A case study for the terrestrial
1018 late Miocene. *Earth and Planetary Science Letters*, 271(1), 53-62.
1019 <https://doi.org/10.1016/j.epsl.2008.03.035>
- 1020 Lyle, M., Dadey, K. A., & Farrell, J. W. (1995). 42. The Late Miocene (11–8 Ma) Eastern
1021 Pacific Carbonate Crash: evidence for reorganization of deep-water Circulation by the
1022 closure of the Panama Gateway. *1995 Proceedings of the Ocean Drilling Program,*
1023 *Scientific Results*, 138.
- 1024 Mayk, D., Fietzke, J., Anagnostou, E., & Paytan, A. (2020). LA-MC-ICP-MS study of boron
1025 isotopes in individual planktonic foraminifera: A novel approach to obtain seasonal
1026 variability patterns. *Chemical Geology*, 531. Article.
1027 <https://doi.org/10.1016/j.chemgeo.2019.119351>
- 1028 Müller, P. J., Kirst, G., Ruhland, G., Von Storch, I., & Rosell-Melé, A. (1998). Calibration of the
1029 alkenone paleotemperature index U₃₇K' based on core-tops from the eastern South
1030 Atlantic and the global ocean (60 N-60 S). *Geochimica et Cosmochimica Acta*, 62(10),
1031 1757-1772. [https://doi.org/10.1016/S0016-7037\(98\)00097-0](https://doi.org/10.1016/S0016-7037(98)00097-0)
- 1032 Nairn, M. (2018). *Mid-Late Miocene climate constrained by a new Laser Ablation ICP-MS set*
1033 *up*. Cardiff University,
- 1034 Nürnberg, D., Bijma, J., & Hemleben, C. (1996). Assessing the reliability of magnesium in
1035 foraminiferal calcite as a proxy for water mass temperatures. *Geochimica et*
1036 *Cosmochimica Acta*, 60(5), 803-814.
- 1037 Pagani, M., Freeman, K. H., & Arthur, M. A. (1999). Late Miocene Atmospheric
1038 CO₂ Concentrations and the Expansion of C₄ Grasses.
1039 *Science*, 285(5429), 876-879. <https://doi.org/10.1126/science.285.5429.876>
- 1040 Pearson, P. N., & Burgess, C. E. (2008). Foraminifer test preservation and diagenesis:
1041 comparison of high latitude Eocene sites. *Geological Society, London, Special*
1042 *Publications*, 303(1), 59-72. <https://doi.org/10.1144/SP303.5>
- 1043 Pearson, P. N., Ditchfield, P. W., Singano, J., Harcourt-Brown, K. G., Nicholas, C. J., Olsson, R.
1044 K., et al. (2001). Warm tropical sea surface temperatures in the Late Cretaceous and
1045 Eocene epochs. *Nature*, 413(6855), 481-487. <https://doi.org/10.1038/35097000>
- 1046 Pena, L., Calvo, E., Cacho, I., Eggins, S., & Pelejero, C. (2005). Identification and removal of
1047 Mn–Mg–rich contaminant phases on foraminiferal tests: Implications for Mg/Ca past
1048 temperature reconstructions. *Geochemistry, Geophysics, Geosystems*, 6(9).
1049 <https://doi.org/10.1029/2005GC000930>
- 1050 Petersen, J., Barras, C., Bézou, A., La, C., De Nooijer, L. J., Meysman, F. J. R., et al. (2018). Mn/
1051 Ca intra- and inter-test variability in the benthic foraminifer *Ammonia tepida*.
1052 *Biogeosciences*, 15(1), 331-348. Article. <https://doi.org/10.5194/bg-15-331-2018>

- 1053 Piasias, N., & Mix, A. (1988). *Aliasing of the geologic record and the search for long-period*
1054 *Milankovitch cycles* (Vol. 3).
- 1055 Pound, M. J., Haywood, A. M., Salzmann, U., Riding, J. B., Lunt, D. J., & Hunter, S. J. (2011).
1056 A Tortonian (Late Miocene, 11.61–7.25Ma) global vegetation reconstruction.
1057 *Palaeogeography, Palaeoclimatology, Palaeoecology*, 300(1), 29-45.
1058 <https://doi.org/10.1016/j.palaeo.2010.11.029>
- 1059 Raffi, I., Wade, B.S., Pälike, H., Beu, A.G., Cooper, R., Crundwell, M.P., Krijgsman, W.,
1060 Moore, T., Raine, I., Sardella, R. and Vernyhorova, Y.V. (2020). The Neogene Period. In
1061 Geologic Time Scale 2020, (pp. 1141-1215). Elsevier. [https://doi.org/10.1016/B978-0-](https://doi.org/10.1016/B978-0-12-824360-2.00029-2)
1062 [12-824360-2.00029-2](https://doi.org/10.1016/B978-0-12-824360-2.00029-2).
- 1063 Raitzsch, M., & Hönisch, B. (2013). Cenozoic boron isotope variations in benthic foraminifers.
1064 *Geology*, 41(5), 591-594. <https://doi.org/10.1130/g34031.1>
- 1065 Raitzsch, M., Kuhnert, H., Hathorne, E. C., Groeneveld, J., & Bickert, T. (2011). U/Ca in benthic
1066 foraminifers: A proxy for the deep-sea carbonate saturation. *Geochemistry, Geophysics,*
1067 *Geosystems*, 12(6). <https://doi.org/10.1029/2010GC003344>
- 1068 Rathmann, S., Hess, S., Kuhnert, H., & Mulitza, S. (2004). Mg/Ca ratios of the benthic
1069 foraminifera *Oridorsalis umbonatus* obtained by laser ablation from core top sediments:
1070 Relationship to bottom water temperature. *Geochemistry, Geophysics, Geosystems*, 5(12).
1071 <https://doi.org/10.1029/2004gc000808>
- 1072 Reichart, G.-J., Jorissen, F., Anschutz, P., & Mason, P. R. (2003). Single foraminiferal test
1073 chemistry records the marine environment. *Geology*, 31(4), 355-358.
1074 [https://doi.org/10.1130/0091-7613\(2003\)031](https://doi.org/10.1130/0091-7613(2003)031<0355:SFTCRT>2.0.CO;2)
<0355:SFTCRT>2.0.CO;2
- 1075 Rosenthal, Y., Boyle, E. A., & Slowey, N. (1997). Temperature control on the incorporation of
1076 magnesium, strontium, fluorine, and cadmium into benthic foraminiferal shells from
1077 Little Bahama Bank: Prospects for thermocline paleoceanography. *Geochimica et*
1078 *Cosmochimica Acta*, 61(17), 3633-3643.
- 1079 Rousselle, G., Beltran, C., Sicre, M.-A., Raffi, I., & De Rafélis, M. (2013). Changes in sea-
1080 surface conditions in the Equatorial Pacific during the middle Miocene–Pliocene as
1081 inferred from coccolith geochemistry. *Earth and Planetary Science Letters*, 361, 412-
1082 421. <http://dx.doi.org/10.1016/j.epsl.2012.11.003>
- 1083 Russell, A. D., Hönisch, B., Spero, H. J., & Lea, D. W. (2004). Effects of seawater carbonate ion
1084 concentration and temperature on shell U, Mg, and Sr in cultured planktonic
1085 foraminifera. *Geochimica et Cosmochimica Acta*, 68(21), 4347-4361.
1086 <https://doi.org/10.1016/j.gca.2004.03.013>
- 1087 Sadekov, A., Eggins, S. M., De Deckker, P., & Kroon, D. (2008). Uncertainties in seawater
1088 thermometry deriving from intratest and intertest Mg/Ca variability in *Globigerinoides*
1089 *ruber*. *Paleoceanography*, 23(1). <https://doi.org/10.1029/2007pa001452>
- 1090 Sadekov, A. Y., Eggins, S. M., & De Deckker, P. (2005). Characterization of Mg/Ca
1091 distributions in planktonic foraminifera species by electron microprobe mapping.
1092 *Geochemistry, Geophysics, Geosystems*, 6(12). <https://doi.org/10.1029/2005GC000973>
- 1093 Schiebel, R., & Hemleben, C. (2017). *Planktic Foraminifers in the Modern Ocean*.

- 1094 Schlitzer, R., Ocean Data View, odv.awi.de, (2018).
- 1095 Seki, O., Schmidt, D., Schouten, S., C. Hopmans, E., Sinninghe-Damste, J., & D. Pancost, R.
1096 (2012). *Paleoceanographic changes in the Eastern Equatorial Pacific over the last 10*
1097 *Myr* (Vol. 27).
- 1098 Sexton, P. F., Wilson, P. A., & Pearson, P. N. (2006). Microstructural and geochemical
1099 perspectives on planktic foraminiferal preservation: “Glassy” versus “Frosty”.
1100 *Geochemistry, Geophysics, Geosystems*, 7(12). <https://doi.org/10.1029/2006GC001291>
- 1101 Sosdian, S. M., Greenop, R., Hain, M. P., Foster, G. L., Pearson, P. N., & Lear, C. H. (2018).
1102 Constraining the evolution of Neogene ocean carbonate chemistry using the boron
1103 isotope pH proxy. *Earth and Planetary Science Letters*, 498, 362-376.
1104 <https://doi.org/10.1016/j.epsl.2018.06.017>
- 1105 Sosdian, S.M. and Lear, C.H. (2020). Initiation of the Western Pacific Warm Pool at the Middle
1106 Miocene Climate Transition? *Paleoceanography and Paleoclimatology*, 35(12),
1107 e2020PA003920. <https://doi.org/10.1029/2020PA003920>
- 1108 Stewart, D. R. M., Pearson, P. N., Ditchfield, P. W., & Singano, J. M. (2004). Miocene tropical
1109 Indian Ocean temperatures: evidence from three exceptionally preserved foraminiferal
1110 assemblages from Tanzania. *Journal of African Earth Sciences*, 40(3), 173-189.
1111 <https://doi.org/10.1016/j.jafrearsci.2004.09.001>
- 1112 Stoll, H. M., Guitian, J., Hernandez-Almeida, I., Mejia, L. M., Phelps, S., Polissar, P., et al.
1113 (2019). Upregulation of phytoplankton carbon concentrating mechanisms during low
1114 CO₂ glacial periods and implications for the phytoplankton pCO₂ proxy. *Quaternary*
1115 *Science Reviews*, 208, 1-20. <https://doi.org/10.1016/j.quascirev.2019.01.012>
- 1116 Super, J. R., Thomas, E., Pagani, M., Huber, M., O’Brien, C., & Hull, P. M. (2018). North
1117 Atlantic temperature and p CO₂ coupling in the early-middle Miocene. *Geology*, 46(6),
1118 519-522. <https://doi.org/10.1130/G40228.1>
- 1119 Thil, F., Blamart, D., Assailly, C., Lazareth, C. E., Leblanc, T., Butsher, J., & Douville, E.
1120 (2016). Development of laser ablation multi-collector inductively coupled plasma mass
1121 spectrometry for boron isotopic measurement in marine biocarbonates: New
1122 improvements and application to a modern Porites coral. *Rapid Communications in Mass*
1123 *Spectrometry*, 30(3), 359-371. Article. <https://doi.org/10.1002/rcm.7448>
- 1124 van Hinsbergen, D. J., de Groot, L. V., van Schaik, S. J., Spakman, W., Bijl, P. K., Sluijs, A., et
1125 al. (2015). A paleolatitude calculator for paleoclimate studies. *PloS one*, 10(6).
1126 <https://doi.org/DOI:10.1371/journal.pone.0126946>
- 1127 Vetter, L., Kozdon, R., Mora, C. I., Eggins, S. M., Valley, J. W., Hönisch, B., & Spero, H. J.
1128 (2013). Micron-scale intrashell oxygen isotope variation in cultured planktic
1129 foraminifers. *Geochimica et Cosmochimica Acta*, 107, 267-278.
1130 <https://doi.org/10.1016/j.gca.2012.12.046>
- 1131 von der Heydt, A., & Dijkstra, H. A. (2006). Effect of ocean gateways on the global ocean
1132 circulation in the late Oligocene and early Miocene. *Paleoceanography*, 21(1).
1133 <https://doi.org/10.1029/2005pa001149>

- 1134 Wade, B. S., Pearson, P. N., Berggren, W. A., & Pälike, H. (2011). Review and revision of
1135 Cenozoic tropical planktonic foraminiferal biostratigraphy and calibration to the
1136 geomagnetic polarity and astronomical time scale. *Earth-Science Reviews*, 104(1), 111-
1137 142. <https://doi.org/10.1016/j.earscirev.2010.09.003>
- 1138 Yu, J., & Elderfield, H. (2008). Mg/Ca in the benthic foraminifera *Cibicidoides*
1139 *wuellerstorfi* and *Cibicidoides mundulus*: Temperature versus carbonate ion
1140 saturation. *Earth and Planetary Science Letters*, 276(1), 129-139. [https://doi.org/10.1016/
1141 j.epsl.2008.09.015](https://doi.org/10.1016/j.epsl.2008.09.015)
- 1142 Zachos, J. C., Stott, L. D., & Lohmann, K. C. (1994). Evolution of early Cenozoic marine
1143 temperatures. *Paleoceanography*, 9(2), 353-387. <https://doi.org/10.1029/93PA03266>
- 1144 Zhang, Y. G., Pagani, M., & Liu, Z. (2014). A 12-Million-Year Temperature History of the
1145 Tropical Pacific Ocean. *Science*, 344(6179), 84-87.
1146 <https://doi.org/10.1126/science.1246172>
- 1147
- 1148

